High statistics analysis using anisotropic clover lattices: Single hadron correlation functions

Silas R. Beane,[1] William Detmold,[2,3] Thomas C. Luu,[4] Kostas Orginos,[2,3] Assumpta Parreño,[5] Martin J. Savage,[6] Aaron Torok,[1] and André Walker-Loud[2]

(NPLQCD Collaboration)

[1]*Department of Physics, University of New Hampshire, Durham, New Hampshire 03824-3568., USA*
[2]*Department of Physics, College of William and Mary, Williamsburg, Virginia 23187-8795., USA*
[3]*Jefferson Laboratory, 12000 Jefferson Avenue, Newport News, Virginia 23606., USA*
[4]*N Division, Lawrence Livermore National Laboratory, Livermore, California 94551., USA*
[5]*Departament d'Estructura i Constituents de la Matèria and Institut de Ciències del Cosmos, Universitat de Barcelona, E–08028 Barcelona, Spain.*
[6]*Department of Physics, University of Washington, Seattle, Washington 98195-1560., USA*

(Received 7 April 2009; published 16 June 2009)

We present the results of high-statistics calculations of correlation functions generated with single-baryon interpolating operators on an ensemble of dynamical anisotropic gauge-field configurations generated by the Hadron Spectrum Collaboration using a tadpole-improved clover fermion action and Symanzik-improved gauge action. A total of 292, 500 sets of measurements are made using 1194 gauge configurations of size $20^3 \times 128$ with an anisotropy parameter $\xi = b_s/b_t = 3.5$, a spatial lattice spacing of $b_s = 0.1227 \pm 0.0008$ fm, and pion mass of $M_\pi \sim 390$ MeV. Ground state baryon masses are extracted with fully quantified uncertainties that are at or below the $\sim$0.2%-level in lattice units. The lowest-lying negative-parity states are also extracted albeit with a somewhat lower level of precision. In the case of the nucleon, this negative-parity state is above the $N\pi$ threshold and, therefore, the isospin-$\frac{1}{2}$ πN s-wave scattering phase-shift can be extracted using Lüscher's method. The disconnected contributions to this process are included indirectly in the gauge-field configurations and do not require additional calculations. The signal-to-noise ratio in the various correlation functions is explored and is found to degrade exponentially faster than naive expectations on many time slices. This is due to backward propagating states arising from the antiperiodic boundary conditions imposed on the quark propagators in the time direction. We explore how best to distribute computational resources between configuration generation and propagator measurements in order to optimize the extraction of single baryon observables.

DOI: 10.1103/PhysRevD.79.114502 PACS numbers: 12.38.Gc

I. INTRODUCTION

One of the primary goals of lattice QCD (LQCD) is to calculate the properties and interactions of nucleons and, more generally, systems comprised of multiple hadrons. Precise exploration of the simplest multihadron systems has recently become possible with significant advances in computing resources, as well as through algorithmic and theoretical developments. The two-pion system $\pi^+\pi^+$ is the simplest of such multihadron systems to calculate in LQCD, and current computational resources have allowed for a precise determination of the $\pi^+\pi^+$ scattering length [1,2] at the $\sim$1% level. Recently, we have explored systems comprised of up to 12 π^+'s [3,4] and also systems comprised of up to 12 K^+'s [5] for the first time, allowing a determination of the three-π^+ and three-K^+ interactions. In general, a determination of the two-particle scattering amplitude, or multibody interactions, with LQCD requires calculating the energy-eigenvalues of the system in the finite-volume [6–9]. The energy differences between the multiparticle energy-levels in the finite-volume and the sum of the particle masses determines the scattering amplitude or interaction. As processes of interest to low-energy nuclear physics are in the MeV energy-regime, while the masses of the baryons and nuclei are in the GeV regime, the energy-levels in the volume must be determined to high precision to yield useful constraints and predictions for scattering amplitudes, phase-shifts and electroweak properties. Consequently, correlation functions of systems comprised of more than one hadron must be calculated with small statistical and systematic uncertainties ($\ll 1\%$) in order to provide useful information about low-energy nuclear interactions and nuclei.

The correlation functions associated with systems of baryons (and, more generally, states other than the pion) suffer from an exponential degradation of the signal-to-noise ratio as a function of time as argued by Lepage [10]. The scale that dictates this degradation is the difference between the total energy of the baryons in the system and half of the total energy of hadrons that contribute to the correlation function associated with the square of the interpolating operator for the baryon system. An example is provided by the two point nucleon correlator (N is an interpolating field with the quantum numbers of the nu-

cleon) where,

$$\text{signal} \sim \langle N(t)\bar{N}(0)\rangle \overset{t\to\infty}{\to} Ze^{-M_N t},$$
$$\text{noise} \sim \sqrt{\langle N(t)\bar{N}(t)N(0)\bar{N}(0)\rangle} \overset{t\to\infty}{\to} Z' e^{-(3/2)M_\pi t}, \quad (1)$$

neglecting effects of the finite temporal extent which we discuss below (here Z and Z' are overlap factors). Since $M_N - \frac{3}{2}M_\pi > 0$, the signal degrades exponentially in time with this exponent. Further, for multibaryon systems, this exponent is scaled by the baryon number, B, and it consequently requires exponentially larger computational resources to calculate the properties of systems containing $B > 1$ baryons than a single baryon. In many regards, it is this signal-to-noise problem that distinguishes LQCD calculations of quantities typically of importance to nuclear physics from those typically of importance to particle physics.

The main motivation for our present work is to explore very high statistics calculations of the energy spectrum of $B = 0$, 1 correlation functions, quantifying the statistical scaling and identifying any issues that appear in the regime of precision calculations. More generally, we aim to assess the feasibility of extracting precise phase-shifts and multinucleon interactions from multibaryon systems but we leave these discussions to subsequent work. Our focus is on the statistical scaling behavior of these measurements instead of on measuring physically relevant quantities. Consequently, we work with a single ensemble of gauge configurations that was produced by the Hadron Spectrum Collaboration [11,12] (the details of these configurations are discussed below). The analysis presented here enables us to identify a number of issues that will be important to LQCD calculations of quantities where exponentially degrading signal-to-noise ratios are a dominant concern:

(1) While the classic argument of Lepage [10] concerning the behavior of the signal-to-noise ratios of baryon correlation functions seems to be on a solid theoretical footing, it has yet to be explored and verified through direct calculation. We examine the signal-to-noise ratios of the single hadron correlation functions in detail and present a modified version of the Lepage argument that incorporates the finite extent of the temporal direction of the gauge-field configuration, focusing on the case of quark propagators subject to antiperiodic temporal boundary conditions (BCs). Over large regions of the temporal extent of the lattice, the signal-to-noise ratio degrades exponentially faster than expected from the original Lepage argument, see Sec. VIII.

(2) At present, and even more so in the past, the generation of gauge-field ensembles consumes most of the computational resources of LQCD calculations.[1] However, it is not clear what the optimal distribution of computational resources between gauge-field production and measurements (propagator calculations and contractions) is when one is interested in noisy quantities. To address this, we explore what can be accomplished by performing hundreds of measurements per configuration, and how precisely the baryon ground-state masses can be determined from an ensemble of 1194 configurations. We also study whether the measurements ''saturate'' after some critical number have been performed on one configuration (that is, exhibit little or no improvement in uncertainties after a critical number of measurements), finding for baryons that they do not, even up to ~200 measurements per configuration.

(3) Correlation functions that are determined to high precision are amenable to analysis with a variety of techniques, beyond those typically used successfully with low statistics data. On these anisotropic configurations, multiple (five or more) exponential fits to such correlation functions become stable as statistical fluctuations decrease, and the ground state energies can be extracted with high precision. We show that the generalized effective mass (EM) method, in which multiple energies are extracted from a linear system (a method developed by Gaspard Riche de Prony in 1795) also becomes useful for correlation functions with small uncertainties. As two (different but correlated) correlation functions are computed per species of hadron, this method is extended to construct the matrix-Prony method, which is found to be a very clean and effective tool for determining the ground-state energies.

(4) While the correlation function generated by a single-baryon interpolating-operator will be dominated by the baryon ground-state at large times, it also contains contributions from all states that can couple to the operator. This includes multihadron states. The backward propagating component of the nucleon correlation function is dominated by the lowest energy negative-parity $I = \frac{1}{2}$ state for the projection-operator we have applied to the correlation functions. By measuring the energy of this state, which is above the πN threshold and therefore is a continuum state, the phase-shift associated with the s-wave πN interaction is determined at this energy. The important point here is that this process contains disconnected diagrams, which are encoded in the gauge-field configurations, and do not require additional (of order the volume in number) calculations.

(5) We also note that thermal states, while strongly suppressed, are seen in our high precision data. In

[1]For example, the USQCD collaboration used ~60% of its resources for ensemble generation in 2008/9.

these states, some part of the hadronic state propagates backward in time and can consequently manifest itself in the correlation function as an exponential with energy less than that of the zero temperature ground state. These contributions have amplitudes that are exponentially suppressed by the temporal extent of the configuration, but they can be extracted in certain temporal regions of the correlation function(s) where other components are also small. They can lead to pollution of the ground-state signal.

The structure of this work is as follows. Section II introduces the details of the lattice calculations we perform, and in Sec. III we discuss our expectations for the hadron spectrum on this ensemble. Section IV introduces the tools used in our analysis and presents detailed comparisons of the different methods we utilize. Following this, Secs. V, VI, and VII present our main results for the pseudoscalar mesons, ground-state baryons and negative-parity excited states, respectively. In Secs. VIII and IX we discuss the behavior of noise in our measurements and investigate the scaling of uncertainties in hadron masses for varying numbers of gauge configurations and measurements. We conclude in Sec. X. In subsequent works, we will address states with baryon number, $B > 1$.

II. LATTICE QCD CALCULATIONS

A. Calculational details

In this study, we employ an ensemble of the $n_f = 2 + 1$-flavor anisotropic clover gauge-field configurations that are currently being produced by the Hadron Spectrum Collaboration [11,12]. These ensembles are being generated with dynamical tadpole-improved clover fermions and a Symanzik-improved gauge action (see Ref. [11,12] for full details). All of the calculations that we present here were performed on a single ensemble of gauge-field configurations of size $20^3 \times 128$ with an anisotropy parameter of $\xi = b_s/b_t = 3.5$, a spatial lattice spacing of $b = b_s = 0.1227 \pm 0.0008$ fm, a pion mass of $M_\pi \sim 390$ MeV and a kaon mass of $M_K \sim 546$ MeV. The ensemble used in this study contains 1194 configurations taken at intervals of 10 trajectories, after allowing 1000 trajectories for thermalization. Reference [11] provides a comprehensive analysis of autocorrelation times and thermalization. Some correlation is seen to be present between configurations separated by 30 trajectories.

The light and strange quark-propagators were computed using the same fermion action used in the gauge-field generation. We use the clover discretization of the fermion action as it requires significantly less computational resources than, for instance, the Domain-Wall discretization, in both the production of gauge-field configurations and in the calculation of quark-propagators, while retaining an $\mathcal{O}(b)$-improved spectrum. Unlike the Domain-Wall discretization, the Clover discretization does not have a lattice chiral symmetry. At moderate lattice spacings, this may significantly impact the extraction of the properties and interactions of pions and kaons, but it is not expected to produce systematic uncertainties that are as significant in the properties and interactions of baryons (this remains to be verified and will not be addressed here).

The quark propagators are calculated with antiperiodic BC's imposed on the time direction and periodic BCs imposed on the spatial directions. As multiple propagators are calculated on each configuration, iterative solvers beyond the simple conjugate gradient algorithm can provide significant speed improvements. In particular, we employ the deflated conjugate gradient algorithm proposed in Ref. [13], and implemented in the `Chroma` lattice field theory library [14] as the `EigCG` inverter. In our typical production runs, we compute from 30 to 100 propagators in sequence, observing a factor of ~7 improvement in inversion speed after the first few solves are used to deflate low-lying eigenvalues from subsequent inversions. Figure 1 shows the details of the propagators computed in this work. The histogram indicates the number of propagators computed on each of the 1194 configurations (averaged over four adjacent configurations for clarity). The total number of propagators computed in this data set is 292,500, an average of 245 propagators per configuration (we note that the maximum number of point-to-all propagators that could be computed on each of the configurations is $\sim 10^6$)

Each propagator is generated from a gauge-invariantly Gaussian-smeared source [15,16], on a stout-smeared [17] gauge-field in order to optimize the overlap onto the ground-state hadrons. On each configuration, the locations of the propagator source points are chosen randomly throughout the configuration. In Fig. 2, we show a histogram of the 4d-separation, R, between the each pair of

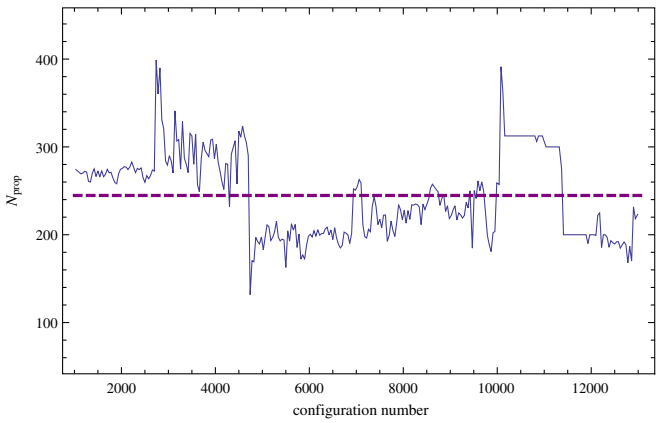

FIG. 1 (color online). The number of propagators, N_{prop}, used in measurements of correlation functions on each configuration used in this study. For the purpose of clarity, bins of four configurations (40 trajectories) have been averaged. The ensemble-average of the number of propagators calculated per configuration, 245, is indicated by the dashed horizontal line.

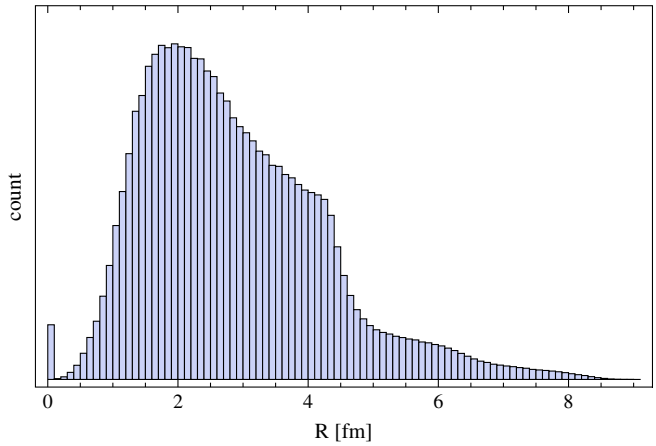

FIG. 2 (color online). The separation between pairs of sources on a given configuration, defined to be the minimum distance between two sources, including the effect of the (anti-) periodic boundary conditions. The height of the bar at $R = 0$ corresponds to the total number of propagators.

sources on each configuration. The shoulder at $R \sim 4$ fm appears because of the (anti) periodic boundary conditions. The average source separation is $\langle R \rangle \sim 2.9$ fm and the source density is 3.43 fm^{-4}.

B. Correlation functions

The propagators are used to compute two-point correlation functions which, for baryons, take the form

$$C_{\mathcal{H};\Gamma}(\mathbf{p}; t) = \sum_{\mathbf{x}} e^{i\mathbf{p}\cdot\mathbf{x}} \Gamma^{\alpha}_{\beta} \langle \mathcal{H}^{\beta}(\mathbf{x}, t) \bar{\mathcal{H}}_{\alpha}(\mathbf{x_0}, 0) \rangle, \qquad (2)$$

where $\mathcal{H}^{\alpha}(\mathbf{x}, t)$ is an interpolating operator for the appropriate baryon state, *e.g.*, for the proton $\mathcal{H}^{\alpha}(\mathbf{x}, t) = \epsilon_{abc}(u^{a,T} C\gamma_5 d^b) u^{c,\alpha}(\mathbf{x}, t)$ where C is the charge conjugation matrix. The Dirac matrix Γ is an arbitrary particle-spin-projector and the point $\mathbf{x_0}$ is the propagator source point. Similar correlation functions are used for the mesons. The interpolating-operator at the source, $\bar{\mathcal{H}}$, is constructed from gauge-invariantly–smeared quark field operators, while at the sink, the interpolating operator is constructed from either local quark field operators, or from the same smeared quark field operators used at the source, leading to two sets of correlation functions. For brevity, we refer to the two sets of correlation functions that result from these source and sink operators as *smeared-point* (SP) and *smeared-smeared* (SS) correlation functions, respectively.

We calculate the smeared-point and smeared-smeared correlation functions associated with the π^+, K^+ ($J^{\pi} = 0^-$) mesons, and the N, Λ, Σ, Ξ ($J^{\pi} = \frac{1}{2}^+$) baryons. For the baryons, the energy projectors $\Gamma_{\pm} = \frac{1}{2}(1 \pm \gamma_0)$ are used to project separately onto either the positive- or negative-energy (parity) states (one of which can be time-reversed and added to the other to improve statistics). Correlation functions associated with a given pair of interpolating fields are averaged over all sources on each configuration, producing one correlation function per interpolating operator pair per configuration.

C. Statistical behavior

Before extracting results for observables, we analyze the statistical behavior of the measured correlators. As the computational cost of each measurement is much less than the computational cost of generating each configuration, performing multiple, $\mathcal{O}(10)$, measurements on each configuration is a practical way to cheaply reduce uncertainties and is an approach that has been used by many groups. Averaging the measurements on a given configuration produces a more accurate estimation of the correlation function on that configuration. *A priori*, one might argue that performing a significantly larger number, say $\mathcal{O}(100$–$1000)$, of measurements on a given configuration is an inefficient use of computing resources as the additional measurements will contain little or no new information and will not decrease the statistical uncertainty in the measurements of interest. This argument is likely true for configurations extending over small volumes. Physically, one expects there are a number of length scales associated with the possible ''saturation'' density of the measurements on a given configuration. As the lightest hadron is the pion, one expects the critical saturation density of measurements to depend parametrically upon the dimensionless quantity ρ/M_{π}^4, where $\rho = N_{\rm src}/V$ where V is the four-volume, and $N_{\rm src}$ is the number of measurements on the configuration. For a simple quantity such as the energy, E, of an eigenstate in the volume, one also expects to find a dependence upon ρ/E^4. For instance, we expect a dependence upon the dimensionless quantity ρ/M_N^4 for the nucleon. Generically, the scale of chiral symmetry breaking, Λ_{χ}, is also expected to enter as ρ/Λ_{χ}^4. Figure 3 shows the scaling of the uncertainty in the effective mass (the logarithm of the ratio of the correlator on adjacent time slices) at one particular time slice for the π^+, K^+, N and Ξ as a function of the number of measurements per configuration. This calculation was performed on 664 of the 1194 configurations in the ensemble, those for which we have made more than 200 measurements. The correlation functions, after being averaged over the sources on each configuration, were blocked in units of 10 configurations (100 trajectories), and the uncertainties in the effective mass (EM) on each time slice were generated with the single omission Jackknife procedure. The π^+ and K^+ correlation functions clearly show deviations from statistical independence beyond $\sim$10 sources per configuration, and by 200 sources per configuration there is little to be gained by performing additional measurements on a configuration. In contrast, measurements of the baryon correlation functions are behaving as if they are statistically independent even

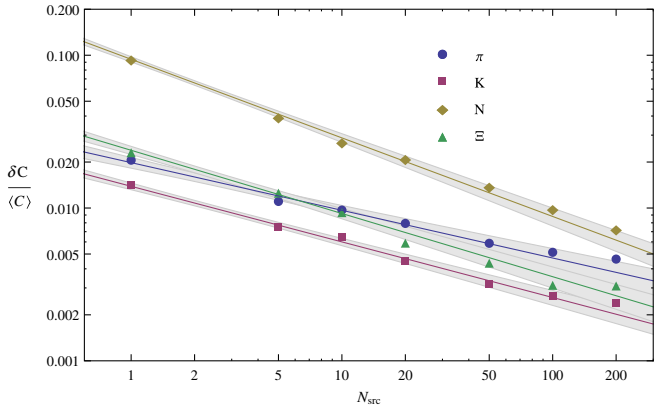

FIG. 3 (color online). A log- log plot of the normalized uncertainty in the mean value of the effective mass of the π^+, K^+, N, and Ξ at time-slice $t = 34$, $t = 34$, $t = 39$, and $t = 49$, respectively, as a function of the number of sources on 664 of the gauge-field configurations (those with more than 200 measurements). The fits correspond to a power-law of the form $\delta C/\langle C\rangle = A(N_{\rm src})^b$. The best fit values for the exponent are $b = -0.31(2)$, $-0.36(1)$, $-0.51(9)$, and $-0.41(5)$ for the π^+, K^+, N, and Ξ, respectively. (Statistically independent measurements would produce $b = -\frac{1}{2}$.)

with 200 sources per configuration. It is clear that the statistical uncertainties in the baryon correlators can be further reduced by performing even more measurements per configuration. These observations are consistent with the arguments regarding the critical source densities.

An alternative way to investigate this question is to consider the correlation between measurements of a correlation function from different sources on the same configuration. A natural quantity to consider is an extension of the standard autocorrelator to a source-to-source autocorrelator, $\chi_{\rm src}$, defined by

$$\chi_{\rm src}(R; t_0) = \Big[\sum_{c,s} C(t_0; c, s)\Big]^{-2}\Big[\sum_{c}\sum_{s_1}\sum_{s_2} C(t_0; s_1, c) \times C(t_0; s_2, c)\theta(s_1, s_2: R)\Big] - 1 \quad (3)$$

where $C(t, c, s)$ is the correlation function of interest evaluated on time-slice t, configuration c and from source s and the function $\theta(s_1, s_2: R)$ is unity if the two sources are separated by a 4d-distance $|s_1 - s_2| < R$. A nonzero value of $\chi_{\rm src}(R)$ indicates the presence of significant correlations over distances shorter than R. We have calculated $\chi_{\rm src}$ for a number of the correlation functions we analyze but find no sign of deviation from zero even for the case of the π^+. This may in part be due to the poor statistics at small source–source separations (see Fig. 2).

A further consideration is that for a given number of configurations, at some value of $N_{\rm src}$, the uncertainty in the measurements of a correlation function on a given configuration will become smaller than the uncertainty in the measurements over the entire ensemble. Once this limit is reached, it is pointless to perform further measurements without also increasing the ensemble size. Our measurements are far from this limit as is illustrated by Fig. 4 where the uncertainties in the measurements of π^+ and N correlation functions on some individual configurations are shown as a function of the number of sources and compared to the overall uncertainty attained with the full ensemble.

An important consideration in generating high statistics measurements is the correlation between configurations. Ideally, enough trajectories separate each gauge-field in the ensemble so that they are statistically independent to the precision of the calculation of interest. The degree of correlation between configurations dictates the number of measurements that should be performed on a given set of

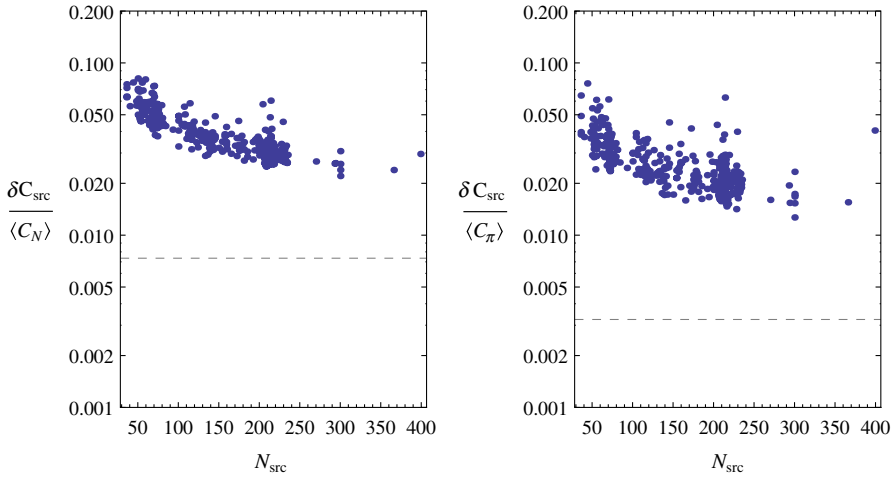

FIG. 4 (color online). The normalized uncertainties in the measurements of N (left panel) and π^+ (right panel) correlation functions for time-slice $t = 10$ are shown for some individual configurations as a function of the number of measurements on that configuration. The dashed lines significantly below the data are the normalized uncertainties on our full ensemble.

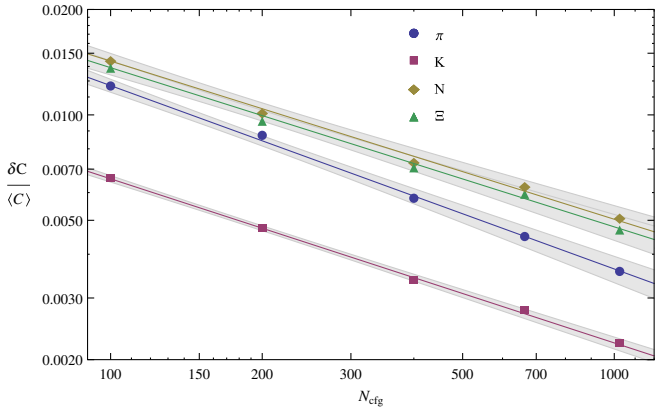

FIG. 5 (color online). A log- log plot of the normalized uncertainty in time-slice $t = 34$, $t = 34$ $t = 29$ and $t = 39$ of the EM of the π^+, K^+, N and Ξ, respectively, as a function of the number of gauge-field configurations, each with 50 measurements. The fits correspond to a power-law of the form $\delta C/\langle C\rangle = A(N_{\rm cfg})^b$. The best fit values are $b = -0.52(1)$, $-0.47(1)$, $-0.45(2)$, and $-0.45(1)$ for the π^+ K^+, N, and Ξ, respectively. (Statistically independent measurements would produce $b = -\frac{1}{2}$.)

configurations before it is more cost effective to enlarge the ensemble. In Fig. 5 we show the uncertainty at given time slices of the EM for the π^+, K^+, N and Ξ as a function of the number of gauge-fields on which 50 measurements are performed. The configurations are maximally separated in Monte Carlo time, but an increasing number of configurations means a reduced separation in Monte Carlo time between each configuration. The curves in Fig. 5 correspond to what is expected for statistically independent configurations. The 100 maximally separated configurations are separated by 80 trajectories, the configurations separated by 20 trajectories appear to be contributing as one expects for statistically independent configurations (assuming that those separated by 80 trajectories are statistically independent). This is consistent with the hadronic autocorrelation times measured on sets of configurations similar to this ensemble in Ref. [11], $\hat{\tau}_\pi \sim \hat{\tau}_N \sim 40$.

D. Computational costs

These calculations required significant computing resources to perform; the total cost of the measurements was approximately 7×10^6 JLab `6n` cluster node hours (this is an older machine with a dual core 3 GHz Pentium D processor per node) distributed over various computational facilities. To put this into context, the generation of the gauge-field configurations required approximately one-third of this time [18]. Our calculational method makes use of hadronic building blocks (partly contracted sets of propagators) which are extremely useful for contracting multiparticle correlation functions but inefficient for single hadron correlation functions; only 4×10^6 JLab `6n` cluster node hours were directly relevant to the calculations presented herein. Nevertheless, it seems that in order to achieve the level of precision of the $B = 1$ correlation functions presented here, propagator generation rather than gauge-field generation is the most computationally intensive component of the LQCD calculation. However, even this will be superseded by the calculation of the contractions that are required for systems involving more than two baryons (the subject of future work).

III. EXPECTED SPECTRA

The form of the correlation functions that are expected to emerge from these calculations is a textbook discussion, but is now becoming more relevant as advances in the field are enabling more complicated processes to be explored, such as scattering, excited states and multihadron interactions. Additionally, the accurate statistical sampling we perform in the current work brings to light features that have been safely neglected in the past. A discussion of the impact of the boundary conditions (here we use antiperiodic temporal BCs for the quark fields) on multiple meson correlation functions that were used in a recent calculation of K^+K^+ scattering can be found in Ref. [5], and a more detailed derivation for a two-particle system can be found in Ref. [19].

For interpolating functions $\mathcal{O}_{A,B}$, the correlation function that is calculated with antiperiodic BCs on the quark-fields is

$$G_{\mathcal{O}}(t) = \frac{1}{Z}\,\mathrm{Tr}[e^{-\hat{H}T}\hat{\mathcal{O}}_A^\dagger(t)\hat{\mathcal{O}}_B(0)] = \frac{1}{Z}\sum_{j,k} e^{-E_jT}e^{(E_j-E_k)t}\langle j|\hat{\mathcal{O}}_A^\dagger(0)|k\rangle\langle k|\hat{\mathcal{O}}_B(0)|j\rangle, \quad (4)$$

where T is the length of the time direction and $Z = \mathrm{Tr}[e^{-\hat{H}T}]$ is the partition function.[2]

As an example, consider the interpolating operator with baryon number zero, strangeness zero ($S = 0$), and isospin equal to two ($I = 2$) that couples to the $\pi^+\pi^+$-state. This state can be written in terms of hadronic field operators as $\hat{\mathcal{O}}(0) = Z_{\pi^+\pi^+}\pi^+\pi^+ + Z_{\pi^+\pi^+\pi^0\pi^0}\pi^+\pi^+\pi^0\pi^0 + \ldots$, where the ellipses denote all other possible hadronic field operators with the same quantum numbers and the Z's are unknown overlap factors. In Eq. (4), this operator thus gives nonzero values for $\langle\pi^-\pi^-|\hat{\mathcal{O}}(0)|0\rangle$, $\langle\pi^-|\hat{\mathcal{O}}(0)|\pi^+\rangle$, $\langle 0|\hat{\mathcal{O}}(0)|\pi^+\pi^+\rangle$, plus all other states with the same quantum numbers as the $\pi^+\pi^+$ source. Consequently the corresponding correlation function contains exponentials e^{-Mt} with energies $M = E_{\pi^+\pi^+}$, $M = E_{\pi^+} - E_{\pi^+} = 0$, $M = -E_{\pi^+\pi^+}$, $M = E_{\pi^+\pi^+\pi^0\pi^0}$, $M = -E_{\pi^+\pi^+\pi^0\pi^0}$, $M = E_{\pi^+\pi^+K^+K^-}$,.... In the zero temperature limit, only

[2]Typically, $\mathcal{O}_A$ and $\mathcal{O}_B$ are closely related; in our calculations, they differ only in the type of smearing of the quark-fields and in the momentum injection.

those exponentials with $M \geq E_{\pi^+\pi^+}$ survive. States with energies less than $E_{\pi^+\pi^+}$ are thermal excitations, for instance arising from the process shown in Fig. 6, and are quite apparent in the measured $I = 2$ $\pi\pi$ correlation functions and have also been observed in hadronic systems involving a static quark [20].

Baryon correlation functions are somewhat different, as the interpolating operator for the single nucleon, for instance, can couple not only to the N, but also to a state containing the N and an even number of π's, to a p-wave ΛK state, to a p-wave ΣK state,to a p-wave $N\pi$ state, and to any other state with the same quantum numbers as the nucleon. Further, it can also couple to backward propagating negative-parity states, such as an s-wave $N\pi$. Finally, the single nucleon interpolating operator can couple forward and backward propagating hadronic states (these are thermal states as they exist only because of the finite temporal extent (temperature) of the configuration), an example being a forward propagating N and a backward propagating π or vice versa. These states are simply illustrated by an example shown in Fig. 7, a $N\pi$ thermal state. Here the finite temporal extent of the configuration is indicated by the vertical lines (these should be (anti-) identified). The two grey regions correspond to the source and sink interpolating field. In the case depicted, the interpolating field at the source is $\bar{N} = (\bar{u}C\gamma_5\bar{d}^T)\bar{u}$ and that at the sink is $N = (u^TC\gamma_5 d)u$, suppressing spin and color indices. For the usual zero temperature ground state, the source produces three valence quarks and the sink annihilates three valence quarks. In the thermal state depicted, the source (right grey region) produces two valence antiquarks and a valence quark (solid lines) while also producing, via gluonic interactions, a sea quark-antiquark pair (dashed line). The three antiquarks between the grey regions combine to form an antinucleon propagating as $\exp(-M_N(T - t))$ where t is the separation between the source and sink and we ignore excited states for simplicity. The quark–antiquark pair propagating around the temporal boundary (since two quarks propagate, the boundary appears periodic at the hadronic level) contribute a factor of

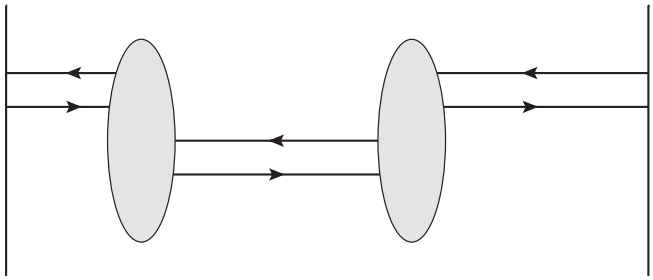

FIG. 6. A depiction of the thermal contribution to $\pi\pi$ correlation function. The vertical lines indicate the antiperiodic temporal boundaries of the configuration and the grey regions represent the $\pi^+\pi^+$ source and sink. The solid lines correspond to valence quark propagators.

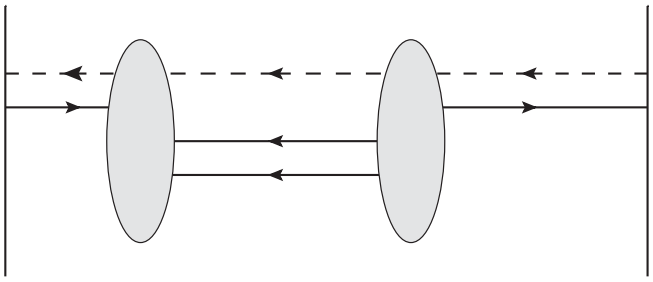

FIG. 7. A depiction of the thermal $\bar{N}\pi$ system produced by the single-nucleon interpolating field. The vertical lines indicate the antiperiodic temporal boundaries of the configuration and the grey regions represent the single-nucleon source and sink. The solid lines correspond to valence quark propagators, while the dashed lines correspond to a sea quark loop from the gauge-field.

$\exp(-M_\pi t)$ where T is the temporal extent of the configuration. The resulting contribution to the two-point correlator is then

$$G(t) \sim Z_{N\bar{\pi}} e^{-M_\pi T} e^{-(M_N - M_\pi)t}, \tag{5}$$

corresponding to a state with energy $M_N - M_\pi$ in the observed spectrum.

In the case of the correlation function resulting from a single nucleon interpolating operator in the A_1 representation of the cubic group, one expects to see a state with energy equal to the N mass, M_N, and also states (a subset of all states) with energy $M_N - 2M_\pi - \delta E_{\pi\pi}$, $M_N + \delta E_{N\pi}$, and $M_N + 2M_\pi + \delta E_{N\pi\pi}$, where $\delta E_{\pi\pi}$ is the interaction energy of two π's in an $I = 0$ state, $\delta E_{N\pi}$ is the interaction energy of the $N\pi$ system, while $\delta E_{N\pi\pi}$ is the interaction energy of the $N\pi\pi$ system. Particularly disturbing is the state with energy $M_N + \delta E_{N\pi}$ corresponding to $N\pi$ moving forward in time and a π moving backwards in time, that conspire to produce a state with an energy that differs from the nucleon mass only by the $N\pi$ interaction energy. Such states will be exponentially suppressed by the temporal extent of the configuration, however, accurately disentangling such states from the zero temperature ground-state will ultimately require calculations on ensembles of gauge-field configurations with different temporal extents.

It is important to realize that thermal states are not simply a curiosity that can be safely ignored. As we shall see in Sec. VIII, they dominate the statistical uncertainty of baryon correlation functions at large times, providing deviations from the naive form of the signal-to-noise ratio. The amplitudes of these states are exponentially suppressed by the temporal extent of the configuration times the mass of the backward going hadronic state. Consequently, the most important thermal states involve backward propagating pions, and, to suppress these states, the product $M_\pi T$ must be large. As the chiral limit is approached this will become more and more difficult since, in the limit, it is impossible to separate any particular state from itself and any number of pions.

TABLE I. Multiexponential fits to smeared-smeared and smeared-point Ξ–correlation functions as a function of the number of exponentials, $N_{\rm exp}$. The number of successful fits, $N_{\rm suc}$ has been defined to be fits with $Q > 0.1$ for a fixed time-length R with a fixed set of initial parameter values. The time window listed is taken as a representative example of a good fit. The first uncertainty is statistical while the second is taken from the standard deviation of successful fits, as defined above.

Ξ										
$b_t M$	$b_t M'$	$N_{\rm exp}$	R: $t_{\rm min}$, .., $t_{\rm max}$	$N_{\rm suc}$	$\tau_{\rm block}$	$\xi_{\rm eff}$	$N_{\rm src}$	$N_{\rm cfg}$	χ^2/dof	Q
0.24138(33)(44)	–	1	20: 47–67	16	1	3.5	245	1194	0.50	1.00
0.24108(28)(10)	0.377(6)(8)	2	45: 24–69	12	1	3.5	245	1194	0.70	0.99
0.24115(24)(07)	0.371(8)(5)	3	50: 14–64	10	1	3.5	245	1194	0.77	0.95
0.24115(25)(07)	0.368(9)(4)	4	50: 10–60	12	1	3.5	245	1194	0.84	0.86

IV. ANALYSIS METHODS

A. Multiexponential fits

The high statistics accumulated for this work allows us to perform stable multiexponential fits using a standard χ^2 minimization. In this section, we explore the determination of the ground and excited states as a function of several variables; the number of exponentials used in the fit function, $N_{\rm exp}$, the range of the fit, R, the number of sources per configuration, the number of configurations, the blocking time $\tau_{\rm block}$, and the (effective) anisotropy, $\xi_{\rm eff}$. We present details of our fits for the Ξ, using a correlated fit to the smeared-smeared and smeared-point correlation functions.

To begin, we performed combined multiexponential fits by minimizing

$$\chi^2 = \sum_{t,t',s,s'} [y_s(t) - C_s(t)](\mathrm{Cov}^{-1})^{s,s'}_{t,t'}[y_{s'}(t') - C'_s(t')], \quad (6)$$

where $y_s(t)$ are the lattice measured correlation functions, $s = [SS, SP]$, and Cov is the covariance matrix between both time slices and correlation functions. The fitting functions used are,

$$C_{SS}(t) = \sum_n Z^S_n Z^S_n e^{-E_n t}, \qquad C_{SP}(t) = \sum_n Z^S_n Z^P_n e^{-E_n t}, \quad (7)$$

where C_{SS} (C_{SP}) denotes the smeared-smeared (smeared-point) correlation function. To perform these fits we start with a single exponential and perform the correlated fit to Z^S_0, Z^P_0 and E_0. A selected set of best fit parameters from this fit are used as initial estimates for the two-exponential fits. This is performed recursively by taking the best fit results from the N exponential fit as an initial estimates to the $N + 1$ exponential fit. With this strategy, successful minimizations with up to six exponentials have been performed. However, with the inclusion of the fifth and higher exponentials, the minimizer performs poorly, and often returns two masses that are degenerate within their uncertainties. Furthermore, as discussed in detail in the previous section, the expected spectrum of states on these anisotropic configurations is such that the resulting masses for the excited states are likely averages of nearby energy levels, see also Sec. IV E below for demonstrations of this. For these reasons, we are only confident in the ground-state energies extracted in these fits. However, the number of exponentials used in a successful minimization plays an important role in minimizing the fitting systematic uncertainty.

The extracted mass of the Ξ as a function of the number of exponentials in the fit form is detailed in Table I. With the high statistics in this study, fitting a single exponential yields a statistical uncertainty of less than 0.2%, with a slightly larger fitting systematic uncertainty, however, 50 time slices must be discarded because of excited state contamination. For our multiexponential fits, the fitting systematic uncertainty is defined to be the standard deviation of all successful fits in a given minimization. To define a successful fit, we take a fixed length in time, $R \equiv t_{\rm max} - t_{\rm min}$, and a fixed set of initial parameters, and keep all fits with an integrated probability distribution $Q > 0.1$ while varying $t_{\rm min}$.[3] One observes that the statistical and systematic uncertainties are not further reduced by including more than three exponentials in the fit. The resulting ground-state mass of the Ξ as a function of the $t_{\rm min}$ used in the fit is shown in upper panel of Fig. 8 (in a style similar to an effective mass plot) with the color and symbol shapes indicating the number of exponentials in the fit. The extraction of the nucleon mass is also shown in the lower panel. Increasing the number of exponentials in the fit, $N_{\rm exp}$, allows the $t_{\rm min}$-interval over which the ground-state energy is seen to plateau to be brought closer to the source where statistical uncertainties are much reduced.

The full set of measurements have been used to generate the fits presented in Table I, and the correlation functions from configurations nearby in Monte Carlo time have not been blocked. Blocking is known to be important, since for correlated configurations, unblocked correlation functions can lead to underestimates of the true uncertainty. For hadronic quantities, we expect that the ensemble we have used has an autocorrelation time of about 40 Monte Carlo time steps [11]. Our calculations have been performed on configurations separated by only $\tau = 10$. Several different

[3]The quality of fit value, Q, is defined as the integrated probability distribution of χ^2 with d degrees of freedom, $Q \equiv \int_{\chi^2_{\rm min}}^{\infty} d\chi^2 \mathcal{P}(\chi^2, d)$, where $\mathcal{P}(x^2, d) = N(x^2)^{d/2-1}\exp(-x^2/2)$, with N the normalization constant. The lower limit of the integration, $\chi^2_{\rm min}$, is the χ^2 of the fit under consideration.

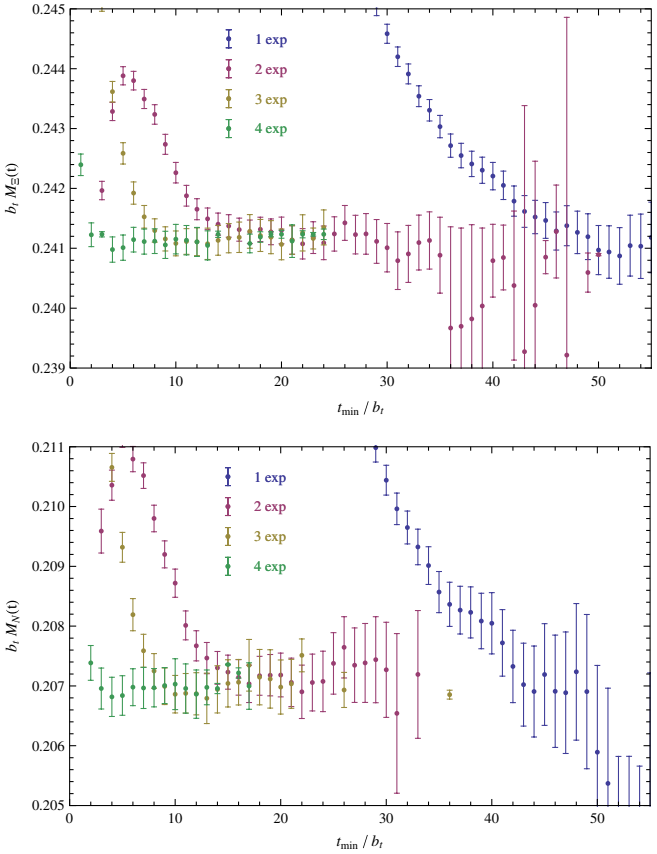

FIG. 8 (color online). The mass of the Ξ (upper panel) and N (lower panel) extracted from multiexponential fits as a function of the t_{min} used in the fit.

fits were performed to determine the effects of blocking on our multiexponential fits, the results of which are collected in Table II. To normalize these fits, a fitting interval, with a range of $R = 30$, was determined from the $N_{exp} = 3$ exponential fits. For these fits, the blocking time τ_{block} has no detectable impact on either the statistical or systematic uncertainties ($\tau_{block} = 1$ corresponds to no blocking, while $\tau_{block} = 10$ corresponds to blocking every 10 configurations).

The range of time used in the fits also plays an important role in minimizing the uncertainty. The resulting fits for short and long time ranges used in three and four exponential fits are shown in Table III. While the range does not have a significant impact on the statistical uncertainty, it does significantly reduce the systematic uncertainty in the fit. To have such long ranges of statistically useful time slices, the anisotropy $\xi = b_s/b_t$, which is 3.5 for this ensemble, is crucial. We have not performed calculations with a different anisotropy (including isotropy), but this can be qualitatively studied by constructing correlation functions using only every second or every third time slice, with an effective anisotropy of $\xi_{eff} = 1.75$ and 1.17, respectively. In the lower section of Table III, we display fits of 1, 2 and 3 exponentials to these reduced sets of measurements. This reduced anisotropy has a significant impact on the resulting uncertainties, particularly for $\xi_{eff} = 1.17$. We were unable to find successful four exponential fits, and the number of successful fits with 1, 2 and 3 exponentials has been reduced. Furthermore, the smaller

TABLE II. Effects of blocking on the determination of the ground-state Ξ mass.

$b_t M$	N_{exp}	R: t_{min}, .., t_{max}	N_{suc}	τ_{block}	ξ_{eff}	N_{src}	N_{cfg}	χ^2/dof	Q
0.24113(25)(36)	3	30: 14–44	17	1	3.5	245	1194	0.84	0.79
0.24130(30)(09)	3	30: 14–44	15	2	3.5	245	1194	0.83	0.81
0.24123(33)(31)	3	30: 14–44	21	5	3.5	245	1194	0.91	0.67
0.24139(34)(34)	3	30: 14–44	11	8	3.5	245	1194	1.1	0.35
0.24063(25)(36)	3	30: 30–60	2	10	3.5	245	1194	0.93	0.62

TABLE III. Effects of fit range, R and anisotropy, ξ_{eff} on the determination of ground-state Ξ mass.

$b_t M$	N_{exp}	R: t_{min}, .., t_{max}	N_{suc}	τ_{block}	ξ_{eff}	N_{src}	N_{cfg}	χ^2/dof	Q
0.24138(33)(44)	1	20: 47–67	16	1	3.5	245	1194	0.50	1.00
0.24108(28)(10)	2	45: 24–69	12	1	3.5	245	1194	0.70	0.99
0.24102(26)(25)	3	24: 20–44	20	1	3.5	245	1194	0.81	0.80
0.24112(26)(15)	4	25: 17–42	15	1	3.5	245	1194	0.94	0.58
0.24113(25)(07)	3	55: 14–69	10	1	3.5	245	1194	0.74	0.98
0.24106(24)(08)	4	60: 9–69	8	1	3.5	245	1194	0.79	0.95
0.24062(49)(29)	1	24: 52, 54, . . . , 74	4	1	1.75	245	1194	0.74	0.78
0.24106(51)(34)	2	24: 34, 36, . . . , 58	11	1	1.75	245	1194	0.55	0.95
0.24111(25)(30)	3	28: 14, 16, . . . , 42	10	1	1.75	245	1194	0.96	0.51
0.24119(37)(30)	1	15: 48, 51, . . . , 63	5	1	1.17	245	1194	0.46	0.9
0.24115(46)(14)	2	24: 33, 36, . . . , 57	2	1	1.17	245	1194	0.72	0.74
0.24110(21)(24)	3	27: 21, 24, . . . , 48	4	1	1.17	245	1194	0.99	0.45

TABLE IV. Effects of the number of sources, $N_{\rm src}$ and number of configurations, $N_{\rm cfg}$ on the determination of the ground-state Ξ mass.

$b_t M$	$N_{\rm exp}$	R: $t_{\rm min}$, .., $t_{\rm max}$	$N_{\rm suc}$	$\tau_{\rm block}$	$\xi_{\rm eff}$	$N_{\rm src}$	$N_{\rm cfg}$	χ^2/dof	Q
0.24304(101)(54)	1	20: 48–68	18	1	3.5	245	120	0.95	0.55
0.24248(64)(24)	1	20: 45–65	22	1	3.5	245	239	0.65	0.96
0.24178(36)(34)	1	20: 43–63	17	1	3.5	245	597	0.66	0.95
0.24110(37)(13)	3	40: 16–46	8	1	3.5	245	239	0.99	0.50
0.24134(24)(17)	3	50: 22–72	16	1	3.5	245	597	0.72	0.98
0.24309(162)(137)	1	20: 43–63	24	1	3.5	1	1025	1.07	0.35
0.24075(129)(44)	1	20: 52–72	24	1	3.5	10	1025	0.72	0.91
0.24063(45)(56)	1	20: 46–56	20	1	3.5	50	1025	0.72	0.91
0.24088(39)(48)	1	20: 46–56	17	1	3.5	100	1025	1.00	0.47
0.24174(72)(60)	3	50: 11–61	13	1	3.5	1	1025	1.10	0.24
0.24116(38)(22)	3	50: 15–65	13	1	3.5	10	1025	0.87	0.81
0.24108(28)(15)	3	50: 15–65	8	1	3.5	50	1025	0.94	0.64
0.24115(30)(04)	3	50: 20–70	3	1	3.5	100	1025	1.15	0.15
0.24138(33)(44)	1	20: 47–67	16	1	3.5	245	1194	0.50	1.00
0.24115(24)(07)	3	50: 14–64	10	1	3.5	245	1194	0.77	0.95

number of time slices in the same physical extent, reduces our ability to control the systematics of the fits.

Finally, the impact of the number of sources, $N_{\rm src}$ and number of configurations $N_{\rm cfg}$, on the uncertainties in the extracted mass of the Ξ has been explored, the results of which are collected in Table IV. With $N_{\rm src} = 50$ or $N_{\rm cfg} = 597$, the statistical uncertainties with $N_{\rm exp} = 3$ exponential fits are the same as with the full set of measurements.[4] However, in both cases the systematic uncertainty is larger than that of the full set of measurements. The corresponding dependence of more complicated multiparticle observables on the number of configurations and sources are under investigation.

For multiexponential fits, it appears that the most important feature in controlling the uncertainty the ground state is the number of exponentials with which a successful minimization can be performed. Neither the statistical nor systematic uncertainties improve beyond the inclusion of three exponentials in the fits. To have confidence in the $N_{\rm exp} = 3$ exponential fits, the anisotropy is found to be essential. A quantitative exploration of the effects of the anisotropy on the stability of multiexponential fits is desirable, but this would be a very costly numerical endeavor. With three or more exponentials, the fitting range, number of sources and number of configurations have essentially the expected effect on the statistical (and systematic) uncertainties.

B. Generalized effective mass plots

Correlation functions on an ensemble of configurations of infinite extent in the time direction become dominated by a single exponential at large times with an argument that is the energy of the ground state of the system,

$$C(t) = \sum_{n=0}^{\infty} Z_n e^{-E_n t} \to Z_0 e^{-E_0 t}. \tag{8}$$

It is conventional to define the effective mass (EM) from the logarithm of the ratio of the correlation function on adjacent time slices. It is also possible[5] to form a more general EM from time slices separated by $t_J > 1$

$$M_{{\rm eff},t_J}(t) = \frac{1}{t_J} \log\left(\frac{C(t)}{C(t+t_J)}\right) \to E_0. \tag{9}$$

For exponentially decreasing signals with time-independent noise, this will naturally reduce the statistical uncertainty in the EM and improve the extraction of energy-eigenvalues as it increases the ''lever-arm'' of the exponential. In such a case, the uncertainty in $M_{\rm eff}(t_J)$ in Eq. (9) will decrease as $1/t_J$. Simple correlation functions involving π's have time-independent uncertainties, but this is not the case for baryonic correlation functions, whose relative uncertainties grow exponentially with time. We explore the improvements to baryon EMs, and ultimately the extraction of baryon masses and the energy-eigenvalues in the volume, that result from $t_J > 1$. In fitting an energy to an EM (and other generalizations), either the Bootstrap or Jackknife procedures are used to generate the covariance matrix associated with the time slices in the range of the fit.[6] This covariance matrix is then used to

[4]The set of measurements with varying numbers of sources has been constructed by including all configurations which have at least $N_{\rm src} = 100$.

[5]This was suggested by K. Juge in a talk at Lattice 2008, see Ref. [21], but may have been used earlier.

[6]In the Bootstrap method, $N_{\rm boot} = N_{\rm cfg}$ randomly generated bootstrap samples are used after blocking over sets of five configurations, while the Jackknife ensembles are constructed by single omission after blocking over 10 configurations. We have found consistent results using both methods and by using different blockings and values of $N_{\rm boot}$.

form the χ^2/dof, which is minimized to determine the energy, and then explored to determine the uncertainty in this energy. The statistical uncertainty is obtained by finding values of the fit parameters where the χ^2 function attains a value of $\chi^2_{\rm min} + 1$.

To demonstrate the impact of $t_J > 1$ for baryon EMs, we examine the smeared-smeared correlation function of the Ξ-baryon. Figure 9 shows the EMs obtained with $t_J = 1$ (left panel) and $t_J = 10$ (right panel). The scatter of the effective mass from time slice to time slice is significantly reduced with $t_J = 10$ compared with $t_J = 1$, allowing for a clear identification of the time range over which it is reasonable to extract the (ground-state) mass of the Ξ. Therefore, the systematic uncertainty associated with the fitting range in the EM is reduced. The statistical uncertainty in the mass of the Ξ extracted from the EMs with the two different values of t_J, when fit over the time time-slice interval, are however very similar, as can be seen in the resulting fits to time-slices $t = 48$ to $t = 58$,

$$\begin{aligned} M_\Xi^{t_J=1} &= 0.24087 \pm 0.00057 \pm 0.00080, \\ \chi^2/\text{dof} &= 0.68, \\ M_\Xi^{t_J=10} &= 0.24060 \pm 0.00061 \pm 0.00060, \\ \chi^2/\text{dof} &= 0.44. \end{aligned} \tag{10}$$

The first uncertainty corresponds to the statistical uncertainty in the mass determined from the χ^2/dof minimization, while the second corresponds to systematic uncertainty associated with the fitting interval. The systematic uncertainty of this fit is determined by varying the fitting interval at each end by 0, ± 1, ± 2 time slices, performing a χ^2/dof minimization over each interval and taking half of the spread of the extracted masses. Alternative procedures such as using fits to rolling windows of time slices within the fitting interval return similar uncertainties.

It is interesting to explore how different values of t_J modify the form of the covariance matrix that is input into the χ^2/dof minimization. The covariance matrices associated with the time-interval $t = 48$ to $t = 51$ from these two EMs are shown in Eq. (11). They are quite different, with the distant off-diagonal elements becoming more significant for increasing t_J.

$$\begin{aligned} \sigma^2_{t_J=1} &= 10^{-7}\begin{pmatrix} 4.82 & 1.97 & 2.71 & 2.70 \\ 1.97 & 6.21 & 3.03 & 3.15 \\ 2.71 & 3.03 & 7.83 & 3.35 \\ 2.70 & 3.15 & 3.35 & 7.06 \end{pmatrix}, \\ \sigma^2_{t_J=10} &= 10^{-7}\begin{pmatrix} 4.75 & 5.09 & 5.29 & 5.26 \\ 5.09 & 5.65 & 5.92 & 5.96 \\ 5.29 & 5.91 & 6.41 & 6.48 \\ 5.26 & 5.96 & 6.48 & 6.90 \end{pmatrix}. \end{aligned} \tag{11}$$

In this comparison, it is important to note that the two extractions make use of different parts of the correlation function. The $t_J = 1$ fit uses five time slices, while the $t_J = 10$ fit uses eight well-separated time slices.

The EMs from the smeared-point Ξ correlation functions with $t_J = 1$ and $t_J = 10$ are shown in Fig. 10. The scatter in the EM for $t_J = 1$ is substantially less than for the smeared-smeared correlation function, as the overlap of the interpolating operator onto the ground state is larger. However, the overlap onto excited states is even larger, and the ground-state component of the correlation function does not become dominant until later times, increasing the fitting systematic uncertainty in the extraction of the ground-state mass.

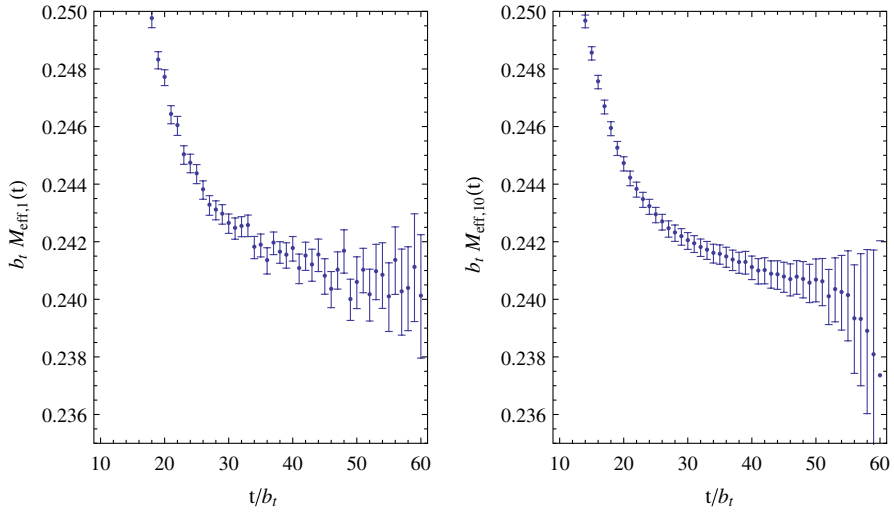

FIG. 9 (color online). The left panel shows the conventional EM ($t_J = 1$) from the smeared-smeared Ξ correlation function, and the right panel shows the EM for the same correlation function with $t_J = 10$.

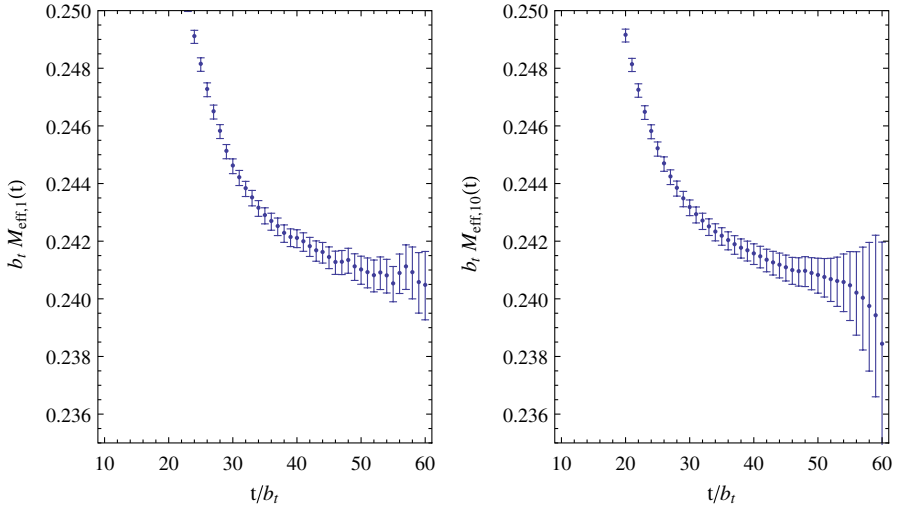

FIG. 10 (color online). The left panel shows the conventional EM ($t_J = 1$) from the smeared-point Ξ correlation function, and the right panel shows the EM for the same correlation function with $t_J = 10$.

C. Prony's method/linear prediction

As the signal-to-noise ratio of baryon correlation functions degrades exponentially with time, it is important to extract the ground-state signal (or excited-state signal if that is the state of interest) from a range of time slices starting at the earliest possible time. Significant effort has been placed into determining interpolating operators that maximize the overlap onto the ground states of the baryons in order to facilitate this. Further, there has been significant effort put into using the variational method [22,23], for which the correlation functions resulting from a number of hadronic interpolating operators are diagonalized on each time slice to give the eigen-energies with the appropriate quantum numbers. A few years ago, Fleming suggested that generalizing the EM-method to two or more exponential functions might be useful in LQCD analysis based on findings of NMR spectroscopists [24].[7] At that time, we explored this method with sets of correlation functions that were available to us at that time, and found the method was quite unstable to the statistical fluctuations in those measurements. More recently, Lin and Cohen [27] and Fleming *et al.* [28] compared this method favorably to the variational approach. Given the small statistical uncertainties in the correlation functions we are presently considering, and the reduction in the systematic uncertainties achieved with $t_J > 1$, we return to explore this method.

In LQCD, two-point correlation functions have the form

$$G(t) = A_0 e^{-\alpha_0 t} + A_1 e^{-\alpha_1 t} + \ldots + A_{k-1} e^{-\alpha_{k-1} t} + \ldots, \tag{12}$$

where t denotes the time slice (time slices are implicitly taken to be evenly-spaced). It follows from Eq. (12) that

$$G(t + nk) + C_{k-1} G(t + n(k-1)) + C_{k-2} G(t + n(k-2)) + .. + C_0 G(t) = 0, \tag{13}$$

where the integer n is the generalization of t_J to the case of a multiexponential function. In order to determine the k coefficients C_i, k equations are required to be formed from the measured correlation function. Given the C_i, the roots of

$$(e^{-n\alpha})^k + C_{k-1}(e^{-n\alpha})^{k-1} + C_{k-2}(e^{-n\alpha})^{k-2} + .. + C_0 = 0, \tag{14}$$

and, in particular, the α's, provide the energies of the states contributing to the correlation function.

1. One-exponential : The standard effective mass

In the case of $k = 1$, where the correlation function is assumed to be a single exponential, and taking $n = 1$,

$$G(t+1) + C_0 G(t) = 0, \qquad (e^{-\alpha}) + C_0 = 0, \tag{15}$$

and the usual expression for the EM follows trivially.

2. Two exponentials

In the case of two exponentials in the correlation function, the most general pair of equations that can be used to extract the two effective masses is

$$G(t + 2n) + C_1 G(t + n) + C_0 G(t) = 0$$
$$G(t + 2n + q_1) + C_1 G(t + n + q_1) + C_0 G(t + q_1) = 0, \tag{16}$$

where q_1 is an arbitrary integer off set between the two equations. Inserting the values of the calculated correlation

[7]The method is more generally referred to as Prony's method [25] after Gaspard Riche de Prony who first constructed it in 1795 [26]. These techniques and other related methods are known as linear prediction theory in the signal analysis community.

function allows for an extraction of $C_{0,1}$ on each time slice, j. These coefficients are then inserted into

$$(e^{-n\alpha})^2 + C_1(e^{-n\alpha}) + C_0 = 0, \tag{17}$$

to recover a numerical values of the $e^{-n\alpha}$. By choosing $n = m = 1$, the expressions of Fleming [24] are recovered. In order to optimize the two-exponential extraction, a search over values of the pair (n, q_1) must be performed. A further systematic uncertainty can be assigned from this choice.

The ground-state extracted from the smeared-smeared Ξ correlation function with $n = q_1 = 5$ is shown in Fig. 11. It is clear that the ground-state signal can be isolated from the correlation function for a large number of time slices, many more than using the single exponential EM (Fig. 9) alone. We have shown the fit to the ground-state result between time-slices $t = 30$ and $t = 60$. The lower-limit of the time interval was chosen to be within an interval for which $\chi^2/\text{dof} < 1$. Extending the fit interval to lower time slices gradually increases the χ^2/dof, as shown in the right panel of Fig. 11, indicating contamination from higher energy states. The upper-limit of the fitting interval was chosen to be in the region for which backward propagating states (due to the antiperiodic BC's in the time direction) were not visible in the EM (or in the χ^2/dof). The ground-state Ξ mass we extract from this 2-exponential analysis is

$$\begin{aligned} M_\Xi &= 0.24109 \pm 0.00043 \pm 0.00057, \\ \chi^2/\text{dof} &= 0.38, \end{aligned} \tag{18}$$

where the first uncertainty is statistical and the second is the fitting systematic (as defined previously). The statistical uncertainty in the 2-exponential extraction is significantly smaller than that obtained from the one-exponential analysis (Eq. (10)). This is due to the substantially increased number of time slices in the ground-state plateau in the generalized EM.

One aspect of this method that is less appealing is the ambiguity in the association of the two roots that result from Eq. (17) to the two states on different time slices and on different jackknife/bootstrap ensembles. This (mis-) identification issue is the cause of the anomalously large uncertainties at time-slices $31, \ldots, 36$ in Fig. 11—this should not be interpreted as variance of the signal for the ground state. Additionally, on different time slices and jackknife/bootstrap ensembles, this method can, and likely will, select different terms in Eq. (12) particularly for the subdominant excited state, adding additional artificial variance to the signals for particular energy eigenstates. Consequently, the extracted second state is not physically meaningful.

3. Three and more exponentials

The generalization of the method to arbitrary numbers of exponential functions is straightforward. In the case of three exponentials, inserting the values of the calculated correlation functions,

$$\begin{aligned} &G(t+3n) + C_2 G(t+2n) + C_1 G(t+n) + C_0 G(t) = 0 \\ &\quad G(t+3n+q_1) + C_2 G(t+2n+q_1) \\ &\quad + C_1 G(t+n+q_1) + C_0 G(t+q_1) = 0 \\ &\quad G(t+3n+q_2) + C_2 G(t+2n+q_2) \\ &\quad + C_1 G(t+n+q_2) + C_0 G(t+q_2) = 0, \end{aligned} \tag{19}$$

with $q_1 \neq q_2 \neq 0$ allows for an extraction of $C_{0,1,2}$ on each

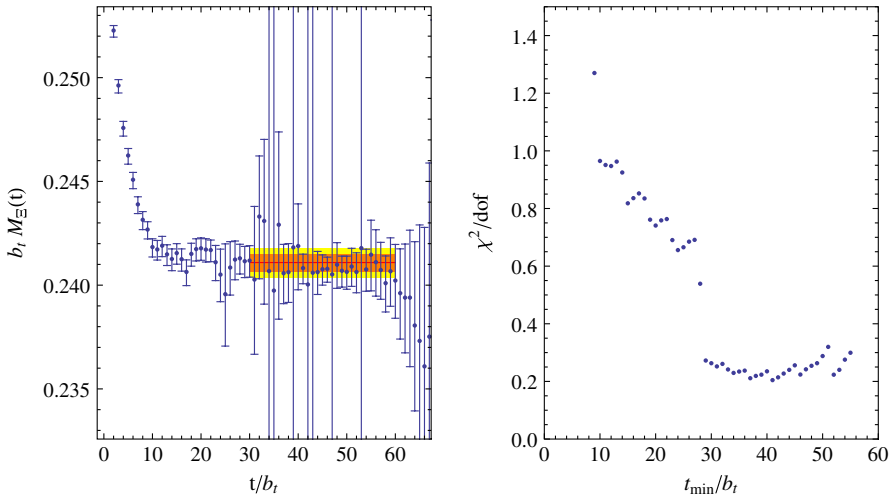

FIG. 11 (color online). The left panel shows the ground-state extracted from the smeared-smeared Ξ correlation function with a 2-exponential Prony determination with $n = q_1 = 5$, and the correlated fit to the time slices between $t = 30$ and $t = 60$. The inner (darker) region corresponds to the statistical uncertainty, while the outer (lighter) region corresponds to the statistical and fitting systematic uncertainties combined in quadrature. The right panel is the χ^2/dof for fits between time-slices $t = t_{\text{min}}$ and $t = 60$.

time slice, t. Again, these coefficients can be extracted uniquely in terms of the $G(t)$ due to the fact that the system is linear. These coefficients $C_{0,1,2}$ are then inserted into

$$(e^{-n\alpha})^3 + C_2(e^{-n\alpha})^2 + C_1(e^{-n\alpha}) + C_0 = 0, \qquad (20)$$

to recover a numerical value of $e^{-n\alpha}$. Analysis of a given correlation function involves searching for the values of the triplet (n, q_1, q_2) that optimizes the extraction (in each equality in Eq. (19), different n can be used). In this case, statistical fluctuations occasionally result in complex roots of Eq. (20) on a particular Jackknife or Bootstrap ensemble. At present, we simply omit these contributions in our analysis. Such complex roots correspond to an oscillatory solution and arise from short distance noise in the correlation function (or nearly degenerate states in the spectrum), and are a well-known issue with the simple Prony method. More advanced methods [29] can mitigate this issue, but do not result in improved extractions of the ground-state so we do not discuss them in detail.

The ground-state energy extracted from the smeared-smeared Ξ correlation function with $n = 10, q_1 = 3, q_2 = 6$ is shown in Fig. 12. It is clear that the ground-state signal is extractable from time slices even closer to the source than with two-exponential analysis. In Fig. 12, the fit to the ground-state between time-slices $t = 10$ and $t = 52$ is shown. The extracted mass is

$$\begin{aligned} M_\Xi &= 0.24124 \pm 0.00032 \pm 0.00034, \\ \chi^2/\mathrm{dof} &= 0.22, \end{aligned} \qquad (21)$$

with the statistical uncertainty being slightly less than in the two-exponential analysis. It is important to realize that this level of precision corresponds to a statistical uncertainty of $\sim$2 MeV in the Ξ mass.

We have successfully applied the four- and five- state Prony method to our data but no improvement is seen beyond the three-exponential extractions.

D. Multi-Correlation function Prony method

There are a number of extensions of the Prony method that exist in the literature (see for example [29]), some of which we have investigated in detail. For the correlation functions we have in hand, these extensions do not significantly improve on the standard Prony method. Typically, these methods are applied in cases where only a single set of measurements is available. However, we have two sets of correlation functions (smeared-smeared and smeared-point) whose energy spectra are identical in the limit of a large number of configurations. It is straightforward to generalize Prony's method to include both correlation functions–the matrix-Prony method. This form leads to a further reduction in the uncertainty of the extraction of the energy eigenvalues. A similar approach, has been briefly discussed in Ref. [28,30].

Assume we have N ($N = 2$ in our case) correlation functions from which we want to extract the energy levels. If these correlation functions are a sum of exponentials they satisfy the following recursion relation,

$$My(\tau + t_J) - Vy(\tau) = 0, \qquad (22)$$

where M and V are $N \times N$ matrices and $y(t)$ is a column vector of N components corresponding to the N correlation functions. Equation (22) implies then the correlation functions are

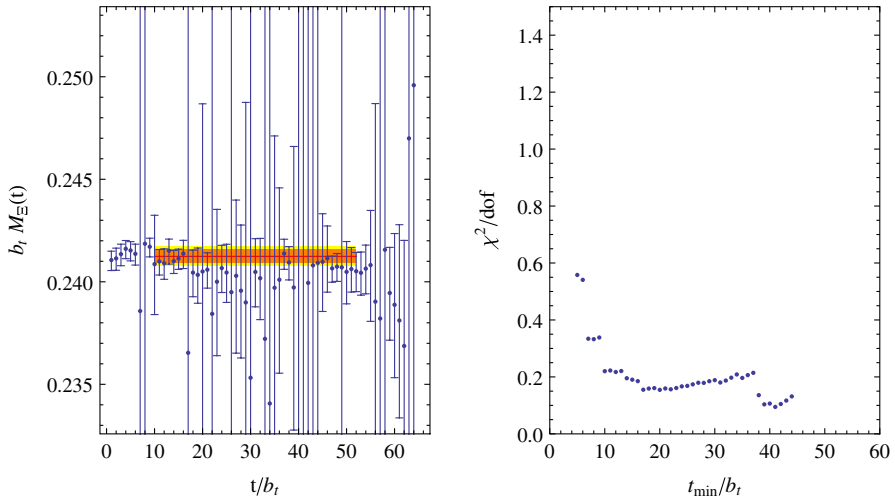

FIG. 12 (color online). The left panel shows the ground-state extracted from the smeared-smeared Ξ correlation function with a 3-exponential Prony determination with $n = 10, q_1 = 3, q_2 = 6$, and the correlated fit to the time slices between $t = 10$ and $t = 52$. The inner (yellow) region corresponds to the statistical uncertainty, while the outer (red) region corresponds to the statistical and fitting systematic uncertainties combined in quadrature. The right panel is the χ^2/dof for fits between the time-slices $t = t_{\mathrm{min}}$ (the horizontal axis) and $t = 52$.

$$y(t) = \sum_{n=1}^{N} C_n q_n \lambda_n^{-t}, \tag{23}$$

where q_n and $\lambda_n = \exp(m_n)$ the eigenvectors and eigenvalues of the following generalized eigenvalue problem

$$Mq = \lambda^{t_J} V q. \tag{24}$$

Given the N sets of correlation functions, the masses can be found by determining the matrices M and V that are needed in order for the signal to satisfy Eq. (22). Solving Eq. (24), then leads to the eigenvalues $\lambda_n = \exp(m_n t_J)$ and the eigenvectors q_n needed to reconstruct the amplitudes each exponential enters the correlation functions. A simple solution can be constructed as follows. First note that

$$M \sum_{\tau=t}^{t+t_W} y(\tau + t_J) y(\tau)^T - V \sum_{\tau=t}^{t+t_W} y(\tau) y(\tau)^T = 0. \tag{25}$$

Clearly, a solution for M and V is

$$\begin{aligned} M &= \left[\sum_{\tau=t}^{t+t_W} y(\tau + t_J) y(\tau)^T \right]^{-1}, \\ V &= \left[\sum_{\tau=t}^{t+t_W} y(\tau) y(\tau)^T \right]^{-1}, \end{aligned} \tag{26}$$

where these inverses exist provided that the range, t_W, is large enough to make the matrices in the brackets full rank ($t_W \geq N - 1$). In our case with two exponentials the range has to be two for achieving full rank. Once the eigenvalues, λ_n and eigenvectors q_n are determined, the amplitudes, C_n, can be reconstructed using t as a normalization point. The shift parameter t_J can be used it improve stability if this is used in conjunction with t_W. The above solution is equivalent to determining M and V by requiring that

$$\Psi^2 = \sum_{\tau=t}^{t+t_W} \langle [My(\tau + t_J) - Vy(\tau)]^T [My(\tau + t_J) - Vy(\tau)] \rangle \tag{27}$$

is minimized. Here, the $\langle \ldots \rangle$ indicate a matrix trace

To go beyond extracting two states, one can construct and solve a second order recursion relation. The minimization condition of Eq. (27) augmented to contain the second order terms in the recursion, can be used to determine the unknown matrices. The resulting eigenvalue problem a second order nonlinear generalized eigenvalue problem which is straightforward to solve. However, to isolate the ground state, which is our present focus, the two state model is sufficient and we do not pursue this further.

To demonstrate how this method works, we return to Ξ correlation function discussed above. Figure 13 shows the generalized EMP for the Ξ mass as a function of time determined with a $N = 2$ matrix-Prony extraction, using both the smeared-smeared and smeared-point correlation functions. The inset shows the second extracted state in addition to the ground state. The extracted value of the Ξ mass, determined by fitting in the time-interval $t = 11$ to $t = 50$, is

$$M_\Xi = 0.24097 \pm 0.00025 \pm 0.00003, \qquad \chi^2/\text{dof} = 0.81, \tag{28}$$

The EM of the dominant state in Fig. 13 plateaus around time-slice $t = 10$, and is well-defined over a large interval. In addition to being somewhat more visually appealing than the previous Prony analyses of single correlation functions, this method provides the smallest uncertainties, particularly for the fitting systematic.

In our final extractions of baryon masses, our EM analysis will use the matrix-Prony method. This method yields ground-state energies that are in complete agreement with those from the other methods discussed. The generalized EMs from the matrix-Prony method are consistently clean, and the quality of fits are uniformly good for the ground state. Since they involve only one fit parameter, one can easily assess the quality of the fits. The procedure for fitting parameters and determining their statistical uncertainty has been described in Sec. IV B. Systematic uncertainties are calculated by performing fits over rolling windows of time slices within the quoted overall range and looking at the standard deviation of the central values of those fits. This is combined in quadrature with a further systematic uncertainty that is generated by sampling a large range of possible values of t_J and t_W and taking the standard deviation of the central values of the resulting fits. The generalized EMP for the Ξ extracted with the matrix-Prony method for a variety of values of t_W and t_J can be seen in Fig. 14.

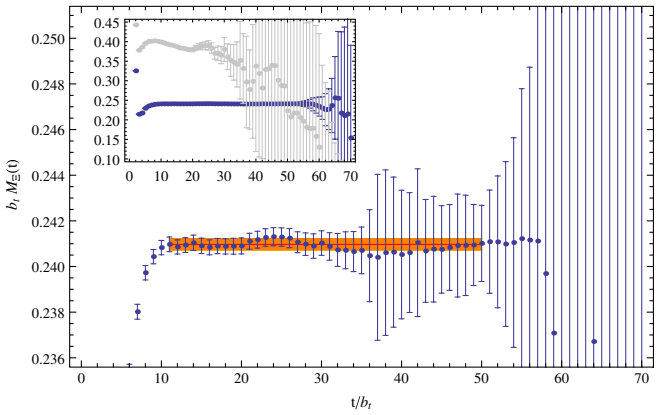

FIG. 13 (color online). The generalized EMP for the mass of the Ξ using a Matrix-Prony analysis with $t_J = 7$ and $t_W = 11$, and the correlated fit to the time slices between $t = 11$ and $t = 50$. The inner (darker) region corresponds to the statistical uncertainty, while the outer (lighter) region corresponds to the statistical and fitting systematic uncertainties combined in quadrature. The inset shows both states extracted with the matrix-Prony method.

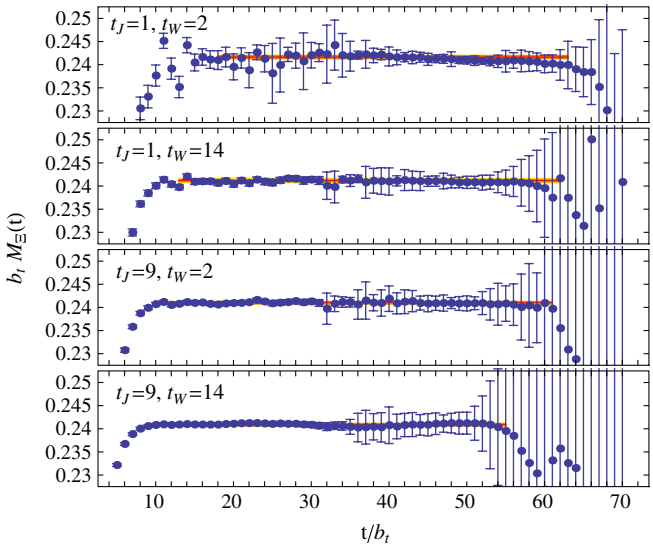

FIG. 14 (color online). The generalized EMP for the mass of the Ξ using a Matrix-Prony analysis for a variety of values for t_J and t_W.

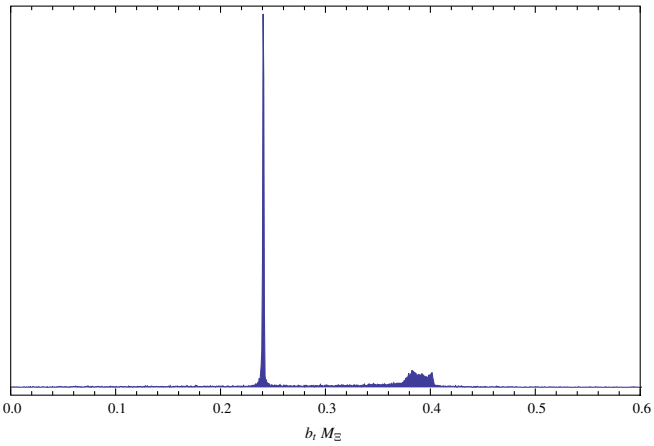

FIG. 15 (color online). The histogram of the positive roots extracted from time-slices $t = 11$ to $t = 50$ from $N = 2$ matrix-Prony analysis of the Ξ correlation functions, with $t_J = 7$ and $t_W = 11$.

E. Prony-Histograms

In extracting the energies of the states through the Prony procedure, a set of roots are produced on each time slice for each member of the Bootstrap or Jackknife ensemble. In general these roots are real and there is an ambiguity in associating the roots with energy-levels in the finite volume (only the single particle masses are approximately known). In order to aid identification of energy-levels it is useful to form histograms of the complete set of roots generated through the Bootstrap procedure. The simplest histogram is formed by accumulating all of the roots obtained on a subset of, or all of, the time slices over all bootstrap/jackknife ensembles. The dominant components of the correlation function will appear as well-defined peaks in the histogram.

In most cases, this histogramming procedure produces very similar results when either two, three or four exponential Prony, or matrix-Prony analyses are used. Only atypically do the higher exponential analyses reveal a clean state that is not present in the two-exponential analysis. Additionally, since our baryon correlation functions are asymmetric in time because of the parity projectors used in Eq. (2), noise is reduced in these histograms by separately accumulating the roots over the two half configuration. As expected, the excited states have a larger presence in the smeared-point correlation function. An example histogram is shown in Fig. 15, corresponding to the Ξ correlation function analyzed in Fig. 13. There is one clear peak in the histogram, corresponding to the Ξ ground-state and one broad structure at higher mass, which the histogram suggests is likely to be a collection of closely-spaced states that currently are not resolvable. This interpretation of the excited state is consistent with expectations for the Ξ spectrum and with the instability of the extractions of the first excited state in the exponential fits discussed earlier.

V. MESON SPECTRUM

The π^+ correlation functions do not suffer from exponential signal-to-noise degradation for configurations of infinite temporal extent (in Sec. VIII, we will find that this is not true for a finite time direction even for the pion). As a result, they can be calculated with small statistical uncertainty on each time slice, as shown in Fig. 16. As the EM for the π^+ does not exhibit a plateau, the π^+ mass is determined by fitting $\cosh(M_\pi(t - \frac{T}{2}))$ to a (large) number of time slices of the correlation function. Performing a double cosh fit to time slices $t = 21$ to $t = 41$ yields

$$\begin{aligned} M_\pi &= 0.06936 \pm 0.00012 \pm 0.00005, \\ \chi^2/\mathrm{dof} &= 0.73, \end{aligned} \tag{29}$$

where the first uncertainty is statistical and the second is fitting systematic. The statistical uncertainty in the mass is determined with the Jackknife procedure, and the fitting systematic is determined by varying the fitting interval over a reasonable range.

The second set of peaks that are visible in the histogram are at an energy consistent with the $I = 1$ $KK\pi$ state (with a threshold at $M_\pi + 2M_K \sim 0.2636$) that can couple to the source that produces a single π^+. With even greater statistics, the energy of this state could calculated with enough precision to extract the $I = \frac{1}{2}$ $K\pi$ and $I = 0$ KK scattering lengths and the $I = 1$ $KK\pi$ three-body interaction. An expression for the energy-levels of this system in a finite-volume in terms of the KK and $K\pi$ scattering amplitudes and various three-body interactions has recently been derived [31] and would be useful in analyzing this

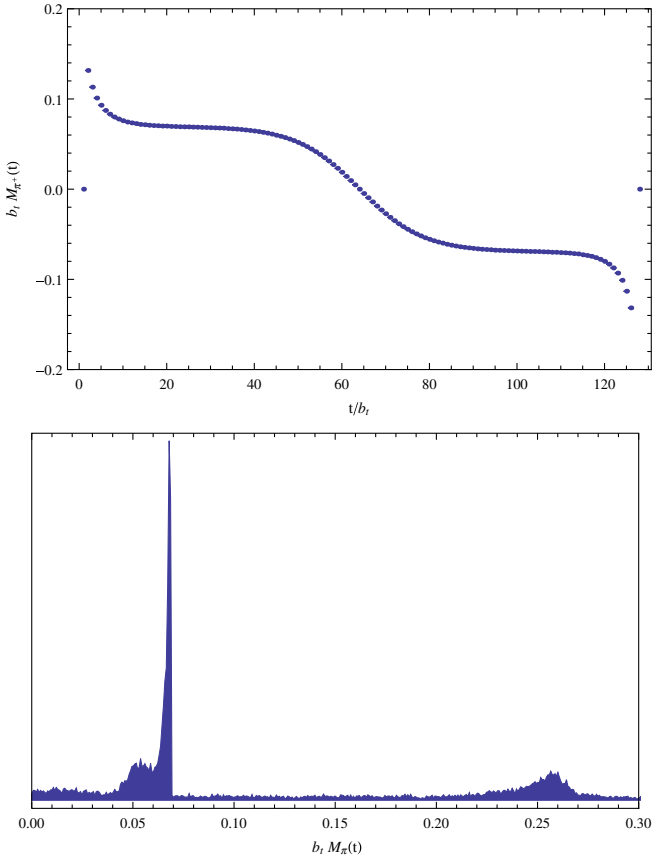

FIG. 16 (color online). The upper panel shows the EM for the smeared-point π^+ correlation function, while the lower panel shows the associated matrix-Prony histogram.

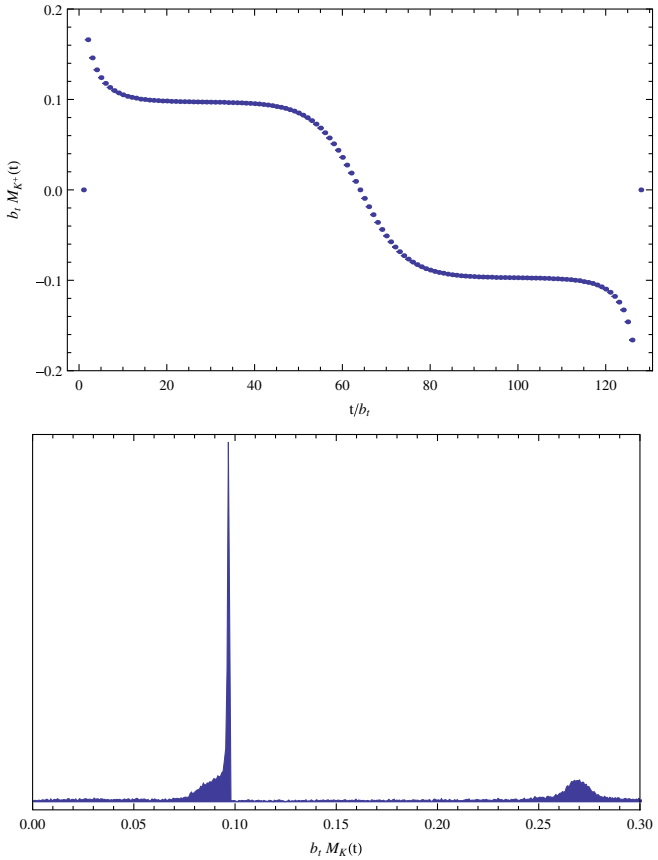

FIG. 17 (color online). The upper panel shows the EM for the smeared-point K^+ correlation function, while the lower panel shows the associated Prony histogram.

state. There is no clear peak that can be associated with $I = 1$ $\pi\pi\pi$, which one would naively thought would have been present. It must be the case that the source does not couple with any appreciable strength to this state.

The EM associated with the smeared-point kaon correlation function is shown in Fig. 17, along with the bootstrap-Prony histogram. Despite the appearance of the EM, no plateau is found in the EM, and the kaon mass is extracted by fitting $\cosh(M_K(t - \frac{T}{2}))$ to a number of time slices of the correlation function. Performing a double cosh fit over the time slices between $t = 29$ and $t = 49$, yields a K^+ mass of

$$M_K = 0.097016 \pm 0.000099 \pm 0.000033, \quad \chi^2/\text{dof} = 1.01. \tag{30}$$

The excited state(s) that are seen in the histogram in Fig. 17 are consistent with the $I = \frac{1}{2}$ KKK. A better measurement of this state, in analogy with the pion correlation function, would allow for a determination of the $I = 0$ KK scattering amplitude.

VI. GROUND-STATE BARYON SPECTRUM

With the methodology we have presented in Sec. IV, we are in a position to extract the masses of the lowest-lying octet baryons. The Ξ correlation functions have been used extensively to demonstrate the strengths and weaknesses of the various methods, with the resulting mass extraction given in Eq. (28), and we do not repeat that discussion here.

The matrix-Prony method applied to the smeared-smeared and smeared-point correlations functions associated with the Σ, Λ and N produces the Prony-histograms and generalized EMs shown in Fig. 18–20. Fitting the Σ EM between time-slices $t = 12$ to $t = 47$ yields Σ mass,

$$M_\Sigma = 0.22811 \pm 0.00028 \pm 0.00018, \quad \chi^2/\text{dof} = 0.77. \tag{31}$$

Fitting the Λ EM between time-slices $t = 12$ to $t = 52$ yields Λ mass,

$$M_\Lambda = 0.22255 \pm 0.00028 \pm 0.00005, \quad \chi^2/\text{dof} = 1.21. \tag{32}$$

Finally, fitting N the EM between time-slices $t = 11$ to $t = 40$ yields N mass,

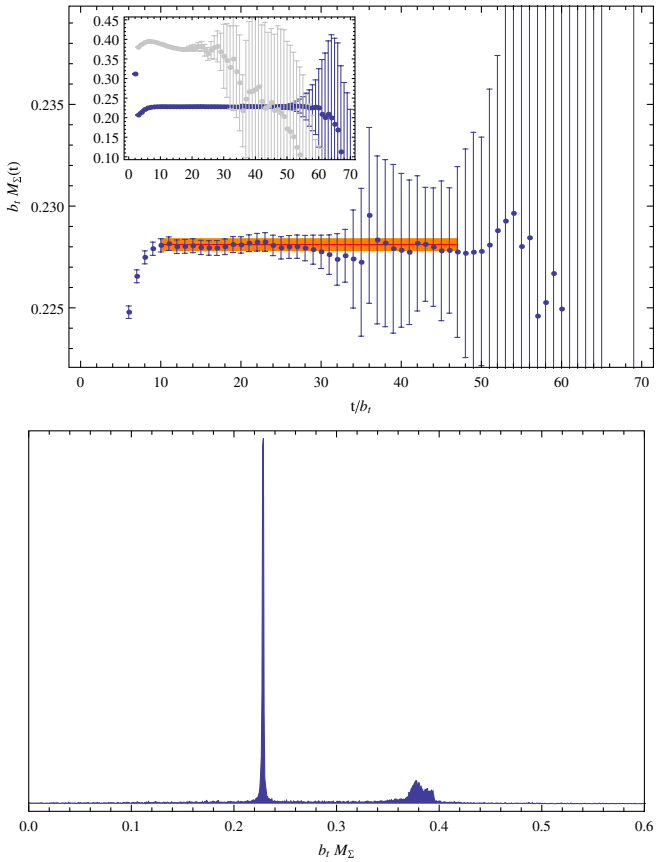

FIG. 18 (color online). The upper panel shows the generalized EM for the mass of the Σ using a matrix-Prony analysis with $t_J = 9$ and $t_W = 17$, and the correlated fit to the time slices between $t = 12$ and $t = 47$. The inner (darker) region corresponds to the statistical uncertainty, while the outer (lighter) region corresponds to the statistical and fitting systematic uncertainties combined in quadrature. The inset show the same ground-state EM plot along with that of the excited state (light points). The lower panel shows the associated Prony histogram of the positive roots for the time-slices $t = 12$ to $t = 47$.

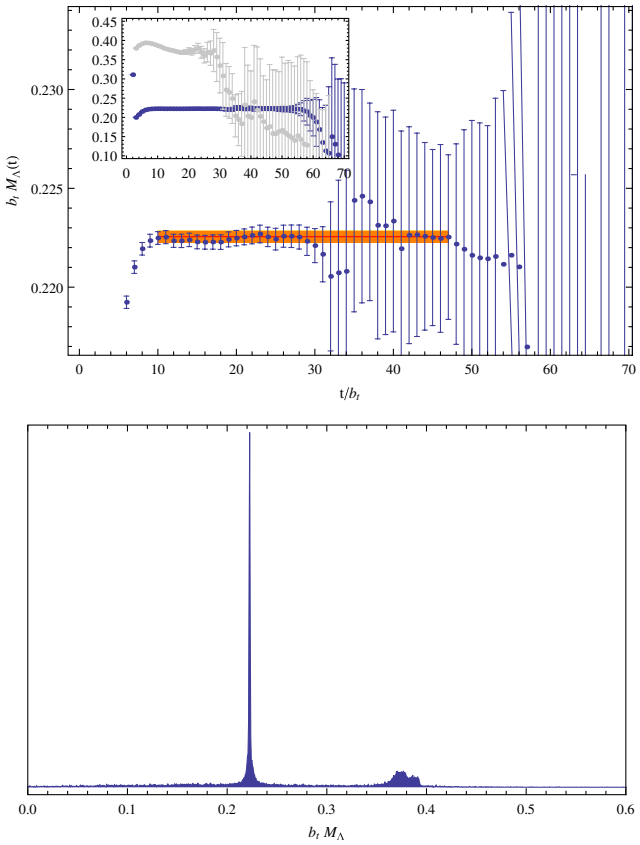

FIG. 19 (color online). The upper panel shows the generalized EM for the mass of the Λ using a matrix-Prony analysis with $t_J = 9$ and $t_W = 11$, and the correlated fit to the time slices between $t = 10$ and $t = 47$. The inner (darker) region corresponds to the statistical uncertainty, while the outer (lighter) region corresponds to the statistical and fitting systematic uncertainties combined in quadrature. The inset show the same ground-state EM plot along with that of the excited state (light points). The lower panel shows the associated Prony histogram of the positive roots for the time-slices $t = 10$ to $t = 47$.

$$M_N = 0.20682 \pm 0.00032 \pm 0.00010, \qquad \chi^2/\mathrm{dof} = 1.5. \tag{33}$$

The results of the best extractions of the ground-state baryon masses using multiexponential fitting and the matrix-Prony method, which give consistent results for each species of baryon, are collected in Table V. These results are completely consistent within their uncertainties, giving us confidence that our extractions are correct.

VII. NEGATIVE-PARITY EXCITED BARYON STATES

The interpolating operators that produce even-parity baryons moving forward in time also produce negative-parity partners moving backwards in time. As the interpolating operators couple to continuum states such as $N\pi$, it is possible that, by using Lüscher's method (and ideally, multiple spatial volumes), the phase-shifts for meson-baryon scattering can be extracted in channels with contributions from disconnected diagrams.

In addition to excited single-baryon states, and the continuum states that carry zero units of momentum in the volume, there are also continuum states where each hadron carries one or more units of momentum in the volume, while having vanishing total momentum. The lowest energy state containing hadrons A and B with back-to-back momenta $\pm\mathbf{p} = \pm\frac{2\pi}{L}\mathbf{n}$ (where $\mathbf{n}$ is an integer triplet) occurs at

$$E_{AB}^{|\mathbf{n}|} = \sqrt{M_A^2 + \left(\frac{2\pi|\mathbf{n}|}{L\xi}\right)^2} + \sqrt{M_B^2 + \left(\frac{2\pi|\mathbf{n}|}{L\xi}\right)^2}. \tag{34}$$

In attempting to unravel the spectrum of states contributing to the correlation functions, we must also consider such continuum states.

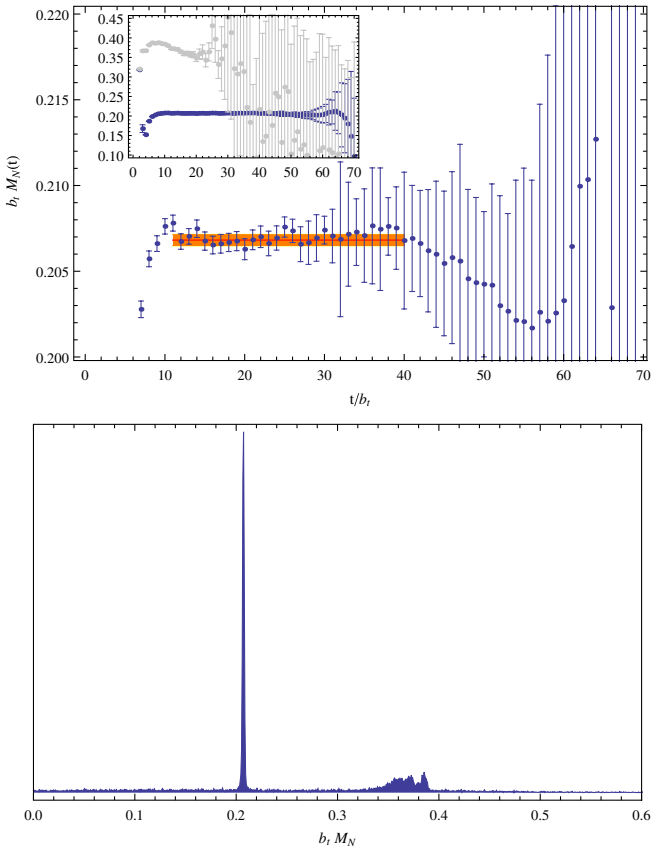

FIG. 20 (color online). The upper panel shows the generalized EM for the mass of the N using a Matrix-Prony analysis with $t_J = 7$ and $t_W = 2$, and the correlated fit to the time slices between $t = 11$ and $t = 40$. The inner (darker) region corresponds to the statistical uncertainty, while the outer (lighter) region corresponds to the statistical and fitting systematic uncertainties combined in quadrature. The inset show the same ground-state EM plot along with that of the excited state (light points). The lower panel shows the associated Prony histogram of the positive roots for the time-slices $t = 11$ to $t = 40$.

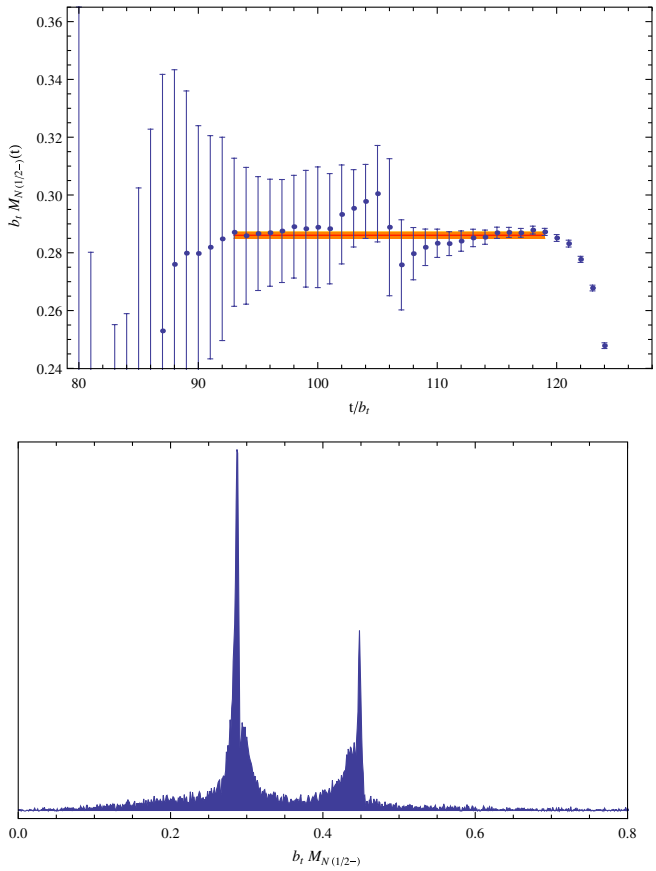

FIG. 21 (color online). The upper panel shows the generalized EM for the lowest-lying negative-parity state coupling to the N-source using a matrix-Prony analysis with $t_J = 5$ and $t_W = 8$, and the correlated fit to the time slices between $t = 93$ and $t = 119$. The inner (darker) region corresponds to the statistical uncertainty, while the outer (lighter) region corresponds to the statistical and fitting systematic uncertainties combined in quadrature. The lower panel shows the associated Prony histogram of the positive roots for the time-slices $t = 93$ to $t = 119$.

The lowest-lying negative-parity state that is expected to couple to the interpolating operator for the single nucleon is the s-wave $N\pi$ state (more precisely, we refer to the A_1^+ representation of the hyper-cubic group), which has a threshold, neglecting interactions, of $M_\pi + M_N = 0.27618 \pm 0.00034 \pm 0.00011$. Fitting the EM shown in Fig. 21 between time-slices $t = 93$ to $t = 119$ yields,

$$E_{N\pi} = 0.2861 \pm 0.0011 \pm 0.0020, \qquad \chi^2/\mathrm{dof} = 0.91, \tag{35}$$

significantly above threshold. Therefore, we conclude that this state is an s-wave πN scattering state with isospin $I = \frac{1}{2}$, as it has energy considerably below that of the first

TABLE V. The ground-state masses of the $J^\pi = \frac{1}{2}^+$ baryons extracted by fitting four exponentials and by the matrix-Prony method. The first uncertainty is statistical while the second is the fitting systematic.

	Exponential Fitting				Matrix-Prony		
state	$b_t M$	range	χ^2/dof	Q	$b_t M$	range	χ^2/dof
N	0.20693(33)(07)	7–64	0.72	0.99	0.20682(32)(10)	11–40	1.50
Λ	0.22265(25)(16)	9–64	0.89	0.78	0.22255(28)(5)	10–47	1.21
Σ	0.22819(25)(07)	8–64	0.85	0.86	0.22811(28)(18)	12–47	0.77
Ξ	0.24112(21)(06)	7–64	0.84	0.87	0.24097(25)(3)	11–50	0.81

momentum excitation in the volume at $E_{N\pi}^{|\mathbf{n}|=1} = 0.33889 \pm 0.00042 \pm 0.00014$, and the $\pi\pi N$ state. Given that there are no other channels that are energetically allowed for this state to mix with, the s-wave πN phase-shift[8] in this channel can be extracted at an energy of $\delta E_{\pi N} = E_{N(1/2^-)} - M_N - M_\pi = 0.0095 \pm 0.0011 \pm 0.0020$ ($\delta E_{\pi N} = 15.3 \pm 1.8 \pm 3.2$ MeV) where the uncertainties are dominated by the uncertainty in $E_{N(1/2^-)}$. It is important to note that this channel receives contributions from disconnected diagrams, and in the calculation we are doing, these contributions are completely accounted for in the gauge-configurations. Using the standard Lüscher procedure, a phase-shift of $\delta_{\pi N} = -26 \pm 7 \pm 6$ degrees is found at this energy. The Prony histogram in Fig. 21 shows significant structure in this channel, and one could argue that there is a single level at $E \sim 0.45$, but this would require further exploration.

For the negative-parity state that couples to the interpolating operators for the Λ, the situation is not so clean. The thresholds for the lowest-lying continuum states, $\Sigma\pi$ and NK, are located at $M_\Sigma + M_\pi = 0.29747 \pm 0.00030 \pm 0.00019$ and $M_N + M_K = 0.30384 \pm 0.00033 \pm 0.00011$, respectively, in the absence of interactions. The corresponding lowest-lying states with one unit of momentum occur at $E_{\Sigma\pi}^{|\mathbf{n}|=1} = 0.35857 \pm 0.00037 \pm 0.00023$, and $E_{NK}^{|\mathbf{n}|=1} = 0.35763 \pm 0.00039 \pm 0.00012$. Fitting the EM shown in Fig. 22 between time-slices $t = 88$ to $t = 117$ yields,

$$\begin{aligned} E_{\Lambda(1/2^-)} &= 0.2983 \pm 0.0008 \pm 0.0004, \\ \chi^2/\text{dof} &= 1.02. \end{aligned} \tag{36}$$

This is, within uncertainties, at the threshold for $\Sigma\pi$ or NK. The eigenstates will be a combination of these two systems and it is likely that we have not resolved the two nearby-states in the EM, and the result in Eq. (36) is actually and average of two closely-spaced energies.

For the lowest-lying negative-parity state(s) produced by the interpolating operator for the Σ, the situation is even more complicated. The threshold of the noninteracting s-wave $\Sigma\pi$ state is at $M_\Sigma + M_\pi = 0.29747 \pm 0.00030 \pm 0.00019$, for the $\Lambda\pi$ state is $M_\Lambda + M_\pi = 0.29191 \pm 0.00030 \pm 0.00007$, and for the NK state is $M_N + M_K = 0.30384 \pm 0.00033 \pm 0.00011$. Therefore, in this large volume, we expect to observe three eigenstates that are nearly degenerate. The lowest-lying states with one unit of momentum occur at $E_{\Sigma\pi}^{|\mathbf{n}|=1} = 0.35857 \pm 0.00037 \pm 0.00023$, $E_{\Lambda\pi}^{|\mathbf{n}|=1} = 0.35341 \pm 0.00030 \pm 0.00007$, and $E_{NK}^{|\mathbf{n}|=1} = 0.35763 \pm 0.00039 \pm 0.00012$ and are well-separated from the $\mathbf{n} = 0$ states. Fitting the EM shown in Fig. 23 between time-slices $t = 95$ to $t = 118$ yields,

$$\begin{aligned} E_{\Sigma(1/2^-)} &= 0.3068 \pm 0.0011 \pm 0.0011, \\ \chi^2/\text{dof} &= 0.80, \end{aligned} \tag{37}$$

in the region where one expects to find three closely-spaced states, corresponding to the eigenstates dominated by $\Sigma\pi$, $\Lambda\pi$, and NK. Given how closely spaced these states are expected to be, the extraction in Eq. (37) is likely a complicated average of three energies.

The situation is no better for the lowest-lying negative-parity states that are expected to couple to the interpolating operator for the Ξ. The lowest-lying s-wave continuum states are $\pi\Xi$, ΛK and ΣK. The threshold for these states, in the absence of interactions, are $E_{\pi\Xi}^{|\mathbf{n}|=\mathbf{0}} = 0.31033 \pm 0.00028 \pm 0.00006$, $E_{K\Lambda}^{|\mathbf{n}|=\mathbf{0}} = 0.31957 \pm 0.00030 \pm 0.00006$, and $E_{K\Sigma}^{|\mathbf{n}|=\mathbf{0}} = 0.32513 \pm 0.00030 \pm 0.00018$, respectively. The corresponding states where both hadrons

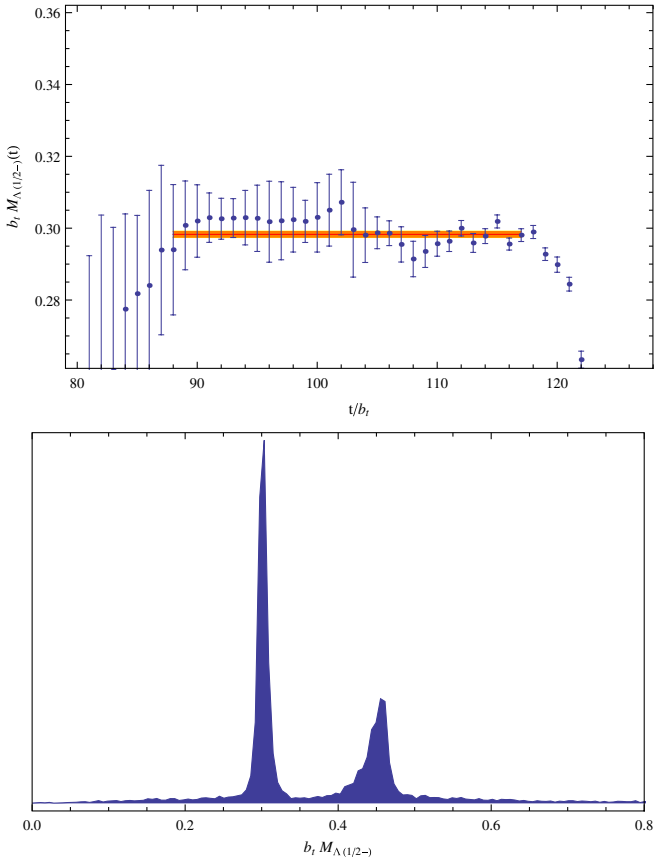

FIG. 22 (color online). The upper panel shows the generalized EM for the lowest-lying negative-parity state coupling to the Λ-source using a matrix-Prony analysis with $t_J = 1$ and $t_W = 5$, and the correlated fit to the time slices between $t = 88$ and $t = 117$. The inner (darker) region corresponds to the statistical uncertainty, while the outer (lighter) region corresponds to the statistical and fitting systematic uncertainties combined in quadrature. The lower panel shows the associated Prony histogram of the positive roots for the time-slices $t = 88$ to $t = 117$.

[8]Here we ignore possible contributions from $L = 4, 6, \ldots$ partial waves that also contribute in the A_1^+ representation of the hyper-cubic group H(4).

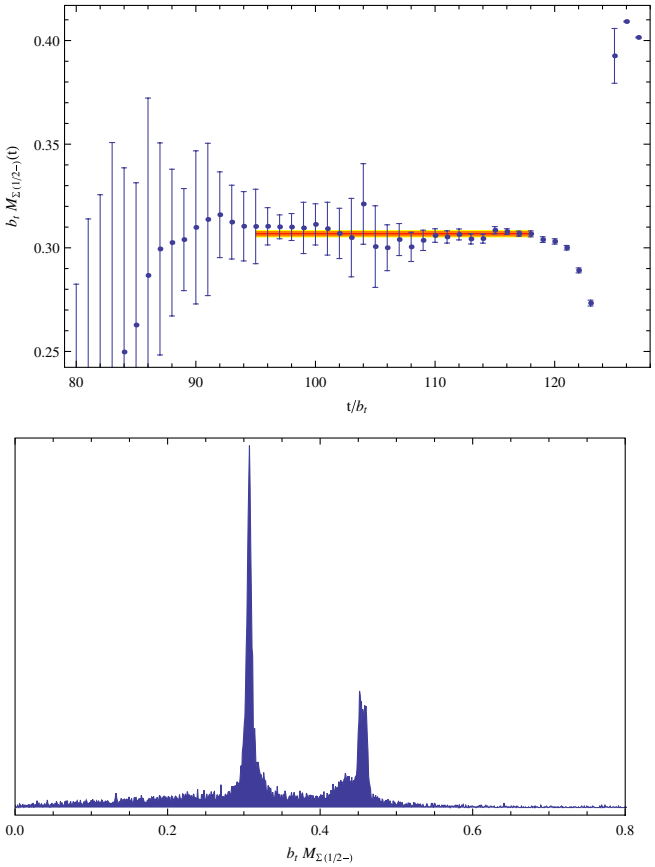

FIG. 23 (color online). The upper panel shows the generalized EM for the lowest-lying negative-parity state coupling to the Σ-source using a Matrix-Prony analysis with $t_J = 7$ and $t_W = 2$, and the correlated fit to the time slices between $t = 95$ and $t = 118$. The inner (darker) region corresponds to the statistical uncertainty, while the outer (lighter) region corresponds to the statistical and fitting systematic uncertainties combined in quadrature. The lower panel shows the associated Prony histogram of the positive roots for the time-slices $t = 95$ to $t = 118$.

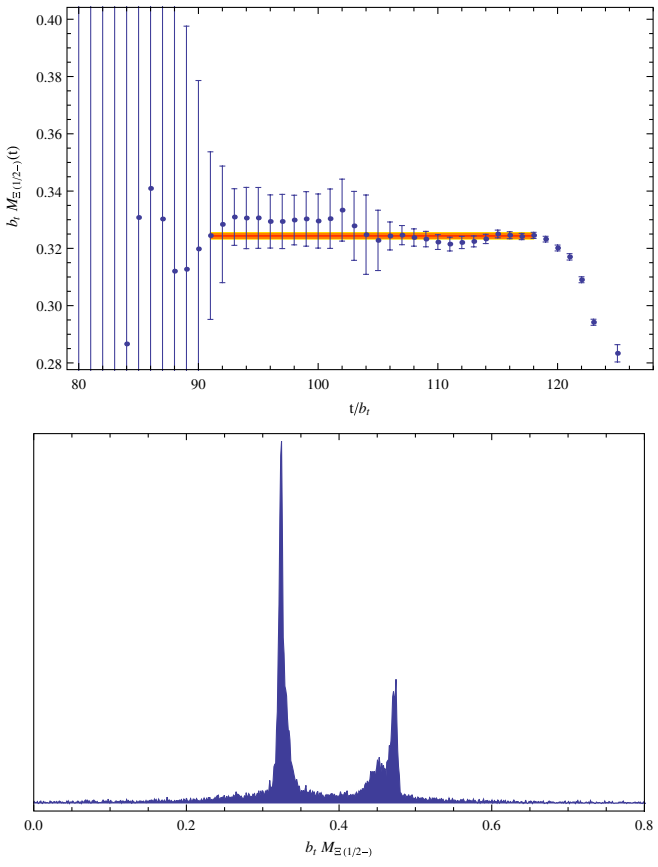

FIG. 24 (color online). The upper panel shows the generalized EM for the lowest-lying negative-parity state coupling to the Ξ-source using a Matrix-Prony analysis with $t_J = 5$ and $t_W = 11$, and the correlated fit to the time slices between $t = 91$ and $t = 118$. The inner (darker) region corresponds to the statistical uncertainty, while the outer (lighter) region corresponds to the statistical and fitting systematic uncertainties combined in quadrature. The lower panel shows the associated Prony histogram of the positive roots for the time-slices $t = 91$ to $t = 118$.

carry one unit of momentum have thresholds state $E^{|\mathbf{n}|=1}_{\Xi\pi} = 0.37058 \pm 0.00033 \pm 0.00007$, $E^{|\mathbf{n}|=1}_{\Lambda K} = 0.37214 \pm 0.00035 \pm 0.00007$, $E^{|\mathbf{n}|=1}_{\Sigma K} = 0.37731 \pm 0.00034 \pm 0.00021$, respectively, Therefore, we expect to observe two sets of three nearly degenerate eigenstates. Fitting the EM shown in Fig. 24 between time-slices $t = 91$ to $t = 118$ yields,

$$E_{\Xi(1/2^-)} = 0.3243 \pm 0.0010 \pm 0.0009, \qquad \chi^2/\mathrm{dof} = 0.72, \tag{38}$$

in the region where one expects to find three closely-spaced states, corresponding to the eigenstates dominated by $\mathbf{n} = 0$ $\Xi\pi$, ΛK, and ΣK. Given how closely spaced these states are expected to be, the extraction in Eq. (38) is

TABLE VI. The masses of the lowest-lying $J^\pi = \frac{1}{2}^-$ states with unit baryon number extracted by fitting three exponentials and by the matrix-Prony method. The first uncertainty is statistical while the second is the fitting systematic.

	Exponential Fitting				Matrix-Prony		
state	$b_t M$	range	χ^2/dof	Q	$b_t M$	range	χ^2/dof
$N(\frac{1}{2}^-)$	0.2871(18)(10)	90–117	1.11	0.28	0.2861(11)(20)	93–119	0.91
$\Lambda(\frac{1}{2}^-)$	0.2954(05)(15)	90–113	0.89	0.64	0.2983(8)(4)	88–117	1.02
$\Sigma(\frac{1}{2}^-)$	0.3074(15)(15)	90–118	1.02	0.41	0.3068(11)(11)	95–118	0.80
$\Xi(\frac{1}{2}^-)$	0.3261(09)(15)	89–115	1.07	0.36	0.3243(10)(9)	91–118	0.72

likely an average of three unresolved energies. There are hints of a couple of other peaks in the Prony-histogram, but nothing conclusive.

The results of the best extractions of the ground-state baryon masses using multiexponential fitting and the matrix-Prony method, which give consistent results for each species of baryon, are collected in Table VI.

VIII. SIGNAL-TO-NOISE RATIOS

Many observables of importance to particle physics that are currently being calculated with LQCD, such as the pion decay constant and the Gasser-Leutwyler coefficients, require the calculation of mesonic correlation functions. Statistical fluctuations on each time slice of these correlation function are well-behaved. In contrast, as argued by Lepage [10], correlation functions involving one or more baryons exhibit exponentially growing statistical noise. In the case of a single positive parity nucleon, the correlation function has the form

$$\langle\theta_N(t)\rangle = \sum_{\mathbf{x}} \Gamma_+^{\beta\alpha} \langle N^\alpha(\mathbf{x}, t)\bar{N}^\beta(\mathbf{0}, 0)\rangle \to Z_0 e^{-M_N t}, \quad (39)$$

where N is an interpolating field that has nonvanishing overlap with the nucleon and the angle brackets indicate statistical averaging over measurements on an ensemble of configurations. The variance of this correlation function is

$$\begin{aligned} N\sigma^2 &\sim \langle\theta_N^\dagger(t)\theta_N(t)\rangle - \langle\theta_N(t)\rangle^2 \\ &= \sum_{\mathbf{x},\mathbf{y}} \Gamma_+^{\beta\alpha}\Gamma_+^{\gamma\delta}\langle N^\alpha(\mathbf{x}, t)\bar{N}^\beta(\mathbf{y}, t)N^\gamma(\mathbf{0}, 0)\bar{N}^\delta(\mathbf{0}, 0)\rangle \\ &\quad - \langle\theta_N(t)\rangle^2 \\ &= Z_{3\pi}e^{-3M_\pi t} + Z_{2N}e^{-2M_N t} + \ldots \to Z_{3\pi}e^{-3M_\pi t}, \quad (40) \end{aligned}$$

and therefore, as Lepage [10] argued, the noise-to-signal ratio behaves as

$$\frac{\sigma}{\bar{x}} = \frac{\sigma(t)}{\langle\theta(t)\rangle} \sim \frac{1}{\sqrt{N}} e^{(M_N - (3/2)M_\pi)t}, \quad (41)$$

at large times (for intermediate times, the overlap factors in Eq. (40) may be such that other components of the noise are dominant; if $|Z_{3\pi}/Z_{2N}| \ll 1$ then the ratio $\sigma/\bar{x}$ will remain constant for a significant temporal extent). More generally, for a system of A nucleons, the noise-to-signal ratio behaves as

$$\frac{\sigma}{\bar{x}} \sim \frac{1}{\sqrt{N}} e^{A(M_N - (3/2)M_\pi)t}, \quad (42)$$

for asymptotic times. Therefore, in addition to the signal itself falling as $G \sim e^{-AM_N t}$, the noise-to-signal associated with the correlation function grows exponentially, as in Eq. (42).

These arguments are constructed for a system with an infinite time direction and are modified in an important way for systems with a finite time direction with given BCs. The calculations that are presented in this work have employed antiperiodic BC's in the time direction. With such BCs the positive parity nucleon correlation function in Eq. (39) becomes

$$\langle\theta_N(t)\rangle \to Z_N e^{-M_N t} + Z_{N\pi} e^{+E_{N\pi}(t-T)}, \quad (43)$$

where $E_{N\pi}$ is the energy of the lowest-lying negative-parity state in the volume, which, for this ensemble of configurations, is a continuum nucleon and pion at rest. The arrow denotes the behavior of the correlation function far from source (in both time directions). Further, the correlation function dictating the behavior of the variance of the nucleon correlation function is modified similarly, with Eq. (40) becoming

$$\begin{aligned} N\sigma^2 \to\ & A_{3\pi} e^{-(3/2)M_\pi T} \cosh\left(3M_\pi\left[t - \frac{T}{2}\right]\right) \\ & + A_\pi e^{-(3/2)M_\pi T} \cosh\left(M_\pi\left[t - \frac{T}{2}\right]\right) \\ & + A_0 e^{-M_N T} + \ldots. \quad (44) \end{aligned}$$

The first term in Eq. (44) arises from 3π's propagating forward and 3π's propagating backwards, the second term arises from 2π's propagating forward along with one π propagating backward and vice versa, the third (time-independent) term arises from a nucleon propagating forward and a nucleon propagating backward, and the ellipses denotes terms involving larger masses. As the negative-parity state is more massive than the nucleon, the nucleon is the dominate component in the correlation function, Eq. (43), for a number of time slices beyond the midpoint of the configuration. From this argument, one expects to see the signal-to-noise ratio degrade even more rapidly than the expectation shown in Eq. (41) in the time slices near the midpoint of the configuration where the correlation function is still dominated by the nucleon. One expects to find regions of the correlation function, depending on the structure of the source, which have the noise-to-signal scaling as $e^{(m_p - (3/2)M_\pi)t}$, $e^{-(1/2)M_\pi T}e^{(m_p-(1/2)M_\pi)t}$, $e^{-M_\pi T}e^{(m_p+(1/2)M_\pi)t}$ $e^{-(3/2)M_\pi T}e^{(m_p+(3/2)M_\pi)t}$, and $e^{m_p(t-T)}$, or combinations thereof.

The high-statistics calculations we are presenting here enables a detailed study of the behavior of the signal-to-noise ratio associated with the correlation functions formed with quark propagators generated with antiperiodic BCs. It is useful to form the effective noise-to-signal plot, in analogy with the EMs. On each time-slice, the quantity

$$\mathcal{S}(t) = \frac{\sigma(t)}{\bar{x}(t)}, \quad (45)$$

is formed, from which the energy governing the exponential behavior can be extracted via

$$E_{\mathcal{S}}(t; t_J) = \frac{1}{t_J}\log\left(\frac{\mathcal{S}(t + t_J)}{\mathcal{S}(t)}\right). \quad (46)$$

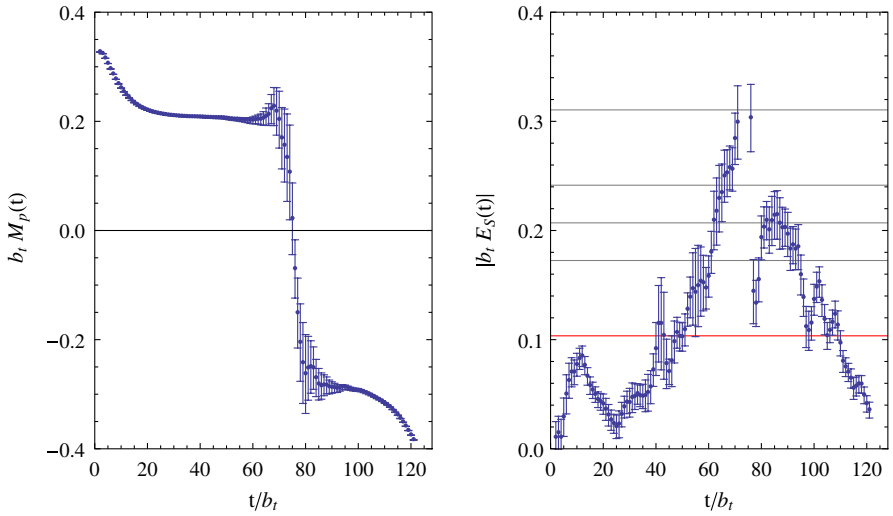

FIG. 25 (color online). The left panel shows the EM of the smeared-point N correlation function formed with with $t_J = 3$. The right panel shows the energy-scale, E_S, associated with the growth of the noise-to-signal ratio, as defined in Eq. (46). The horizontal lines correspond to the energy-scales $m_p - \frac{3}{2}M_\pi$, $m_p - \frac{1}{2}M_\pi$, m_p, $m_p + \frac{1}{2}M_\pi$, and $m_p + \frac{3}{2}M_\pi$ (from lowest energy to highest energy).

If the correlation function is dominated by a single state, and a single energy-scale determines the behavior of the noise-to-signal ratio, the quantity $E_S(t; t_J)$ will be independent of both t and t_J.

In Fig. 25, the full EM of the smeared-point nucleon correlation function is shown (with $t_J = 3$), and in Fig. 26, the full EM of the smeared-smeared nucleon correlation function is shown (with $t_J = 5$). Also shown are the energy-scales associated with the growth of the noise-to-signal ratio from Eq. (46), with uncertainties generated using the Jackknife procedure. Considering the smeared-point correlation function in Fig. 25, after time-slice $t = 35$ or so, the correlation function is dominated by the ground-state nucleon which persists until time-slice $t \sim 70$. Beyond this time slice the backward propagating negative-parity $N\pi$-state becomes dominant. Between time-slices $t \sim 40$ and $t \sim 50$, the noise-to-signal ratio is determined by the expectation of $m_p - \frac{3}{2}M_\pi$. However, after $t \sim 50$ the signal-to-noise ratio degrades exponentially faster than this, and by $t \sim 65$ the relevant energy-scale is $\sim m_p + \frac{1}{2}M_\pi$ and increasing with t. Similar behavior is clear in the smeared-smeared correlation function, for which the nucleon ground state dominates from an earlier time slice.

It is clear from this analysis of the noise-to-signal ratio, that the length of the time direction of these configurations

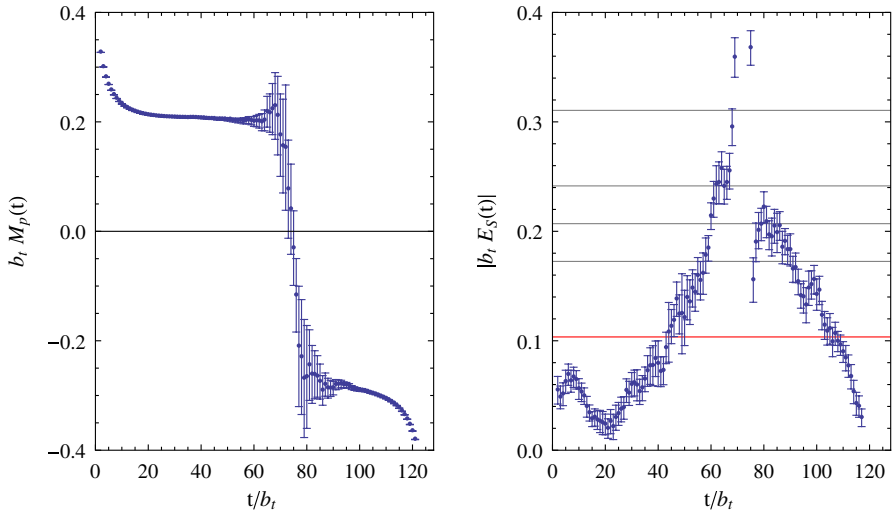

FIG. 26 (color online). The left panel shows the EM of the smeared-smeared N correlation function formed with $t_J = 5$. The right panel shows the energy-scale, E_S, associated with the growth of the noise-to-signal ratio, as defined in Eq. (46). The horizontal lines correspond to the energy-scales $m_p - \frac{3}{2}M_\pi$, $m_p - \frac{1}{2}M_\pi$, m_p, $m_p + \frac{1}{2}M_\pi$, and $m_p + \frac{3}{2}M_\pi$ (from lowest energy to highest energy).

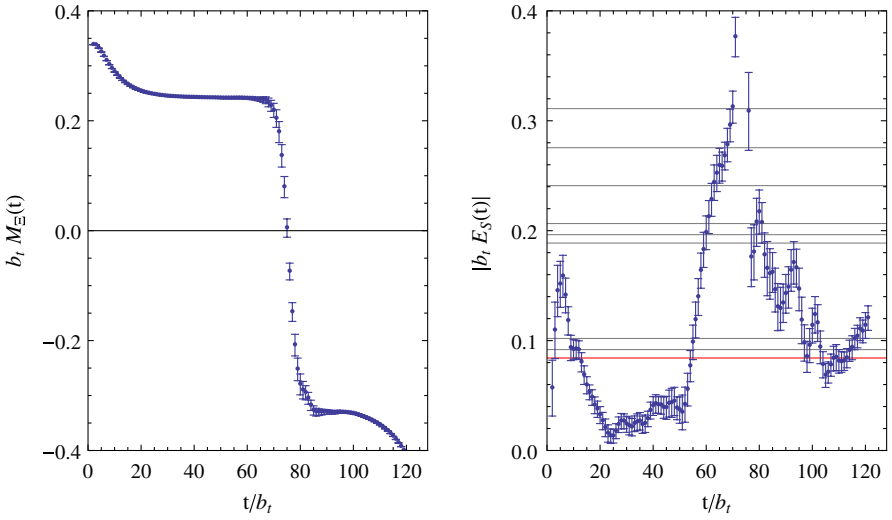

FIG. 27 (color online). The left panel shows the EM of the smeared-point Ξ correlation function formed with $t_J = 3$. The right panel shows the energy-scale, $E_{\mathcal{S}}$, associated with the growth of the noise-to-signal ratio, as defined in Eq. (46). The horizontal lines correspond to the energy-scales $m_\Xi - \frac{3}{2}m_\eta$, $m_\Xi - M_K - \frac{1}{2}m_\eta$, $m_\Xi - m_\eta - \frac{1}{2}M_\pi$, $m_\Xi - \frac{1}{2}m_\eta$, $m_\Xi - M_K + \frac{1}{2}m_\eta$, $m_\Xi - \frac{1}{2}M_\pi$, m_Ξ, $m_\Xi + \frac{1}{2}M_\pi$, and $m_\Xi + m_\eta - \frac{1}{2}M_\pi$ (from lowest energy to highest energy).

and resulting thermal states are limiting the precision of the ground-state nucleon mass determination. This will be even more true for the multiple baryon correlation functions for which the signal-to-noise degrades exponentially faster than in the single-nucleon correlation functions. Increasing the length of the time direction will lead to exponential improvement of the correlation function at large times where the nucleon component dominates the correlation function. It is interesting to note that the coefficients of the backward propagating contributions to the noise-to-signal ratio are suppressed by powers of $e^{-(1/2)M_\pi T}$. On the current configurations with $T = 128$, in order to reduce the contribution to the noise from the $m_p - \frac{1}{2}M_\pi$ component by an order of magnitude, the time extent would need to be increased to $T \sim 192$. This will reduce the $m_p + \frac{1}{2}M_\pi$ component by a factor of $\sim$84 and the $m_p + \frac{3}{2}M_\pi$ component by $\sim$770. Such an increase in the temporal extent would significantly decrease the statistical uncertainties with which ground-state signals are extracted.

The noise-to-signal analysis of the Ξ correlation functions is somewhat more complex, because there are a number of low-lying states which can contribute to the variance. For the $\Xi\bar{\Xi}$ noise correlation function, the light-

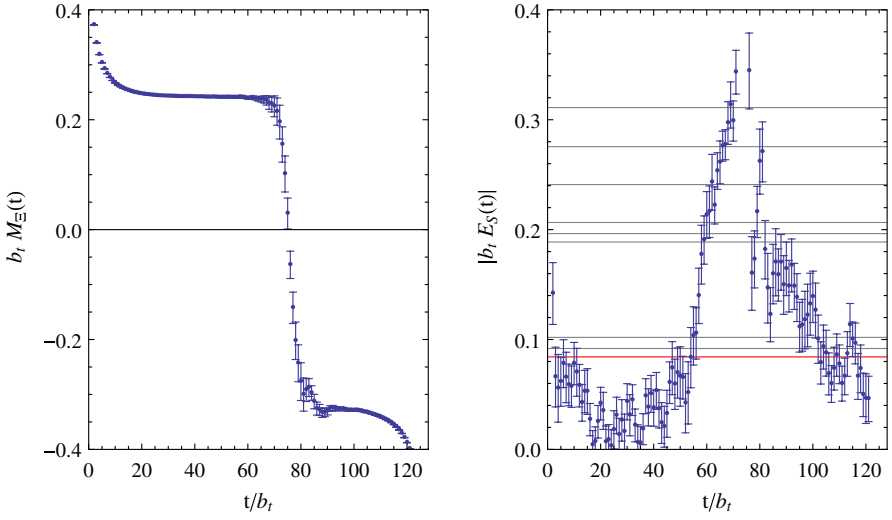

FIG. 28 (color online). The left panel shows the EM of the smeared-smeared Ξ correlation function formed with $t_J = 3$. The right panel shows the energy-scale, $E_{\mathcal{S}}$, associated with the growth of the noise-to-signal ratio, as defined in Eq. (46). The horizontal lines correspond to the energy-scales $m_\Xi - \frac{3}{2}m_\eta$, $m_\Xi - M_K - \frac{1}{2}m_\eta$, $m_\Xi - m_\eta - \frac{1}{2}M_\pi$, $m_\Xi - \frac{1}{2}m_\eta$, $m_\Xi - M_K + \frac{1}{2}m_\eta$, $m_\Xi - \frac{1}{2}M_\pi$, $m_\Xi + \frac{1}{2}M_\pi$, m_Ξ, and $m_\Xi + m_\eta - \frac{1}{2}M_\pi$ (from lowest energy to highest energy).

est intermediate states that can couple to quark-content $ssu\bar{s}\bar{s}\bar{u}$ are $KK\eta$, $\eta\eta\pi$ and $\eta\eta\eta$. The full EMs and the E_S plots for the smeared-point and smeared-smeared Ξ correlation functions are shown in Fig. 27 and 28. In both the smeared-point and smeared-smeared Ξ correlation functions, the noise-to-signal ratio is growing exponentially slower than naive expectations, until about time-slice $t \sim 55$. As the Ξ ground-state dominates the smeared-smeared correlation function beyond $t \sim 40$, this allows for a extraction of the mass with higher precision than expected. This suggests that the noise-source does not couple to the low-lying mesonic states as strongly as expected, and that more massive mesonic states are dominating the noise over many time slices. However, eventually, for $t \gtrsim 55$, the growth of noise overshoots the original Lepage expectation (indicated by the lowest horizontal line in Figs. 27 and 28.

Whilst we are primarily interested in noise in the baryonic sector, it is interesting to note that the mesonic correlation functions also suffer from similar issues. According to the above arguments, the pion correlation function on lattices at zero temperature (infinite temporal extent) will have noise that is independent of time (up to fluctuations) while the kaon will have noise that grows exponentially with the small energy difference $m_K - \frac{1}{2}m_\pi - \frac{1}{2}m_\eta$. However at finite temperature, the noise correlation functions of both systems receive additional contributions that grow faster than the above expectations. This is shown in Fig. 29.

IX. SCALING WITH COMPUTATIONAL RESOURCES

An important component of our current work is to address the future requirements for LQCD calculations in nuclear physics, a field characterized by small energy scales in heavy systems, for example, the 2 MeV binding energy of the ~2 GeV deuteron. In Fig. 30, we show the extracted mass of the π^+, K^+, N and Ξ as a function of the number of configurations in the ensemble for both the exponential and matrix-Prony analysis methods. The full set of measurements performed on each configuration are included, and the fitting intervals are chosen to optimize the extraction for each ensemble size. In each case, the uncertainty in the mass is reduced, as expected, with increasing ensemble size, and the mass extracted from the smaller ensembles tends to be less than that from the larger ensembles. Figure 31 shows the fractional uncertainty in the mass of the π^+, K^+, N and Ξ, associated with the results in Fig. 30, as a function of the number of configurations. An extrapolation can be performed with a fit to the uncertainties in Fig. 31 of the form $\delta M/M = AN_{\mathrm{cfg}}^b$. The exponents extract in these fits are $-0.55(4)$, $-0.51(3)$, $-0.38(4)$, $-0.67(6)$ for the π^+, K^+, N and Ξ, respectively.

The dependence of our results for hadron masses on the number of sources used in the calculations is explored in Fig. 32 where we show the fractional uncertainty in the mass of the π^+, K^+, N and Ξ as a function of the number of sources used on each configuration. In this figure we use an ensemble of 1012 configurations, those on which there are at least 100 measurements. A simple fit of the form $\delta M/M = AN_{\mathrm{src}}^b$ returns exponents $b = -0.03(2)$, $-0.65(19)$, $-0.41(3)$, and $-0.40(6)$ for the π^+, K^+, N, and Ξ, respectively.

The results of this analysis can be simply summarized for baryons (averaging over the nucleon and Ξ) as

$$\frac{\delta M_B}{M_B} \sim \frac{1}{N_{\mathrm{src}}^{0.4} N_{\mathrm{cfg}}^{0.5}}. \tag{47}$$

For mesons, a similar scaling is seen, with a somewhat

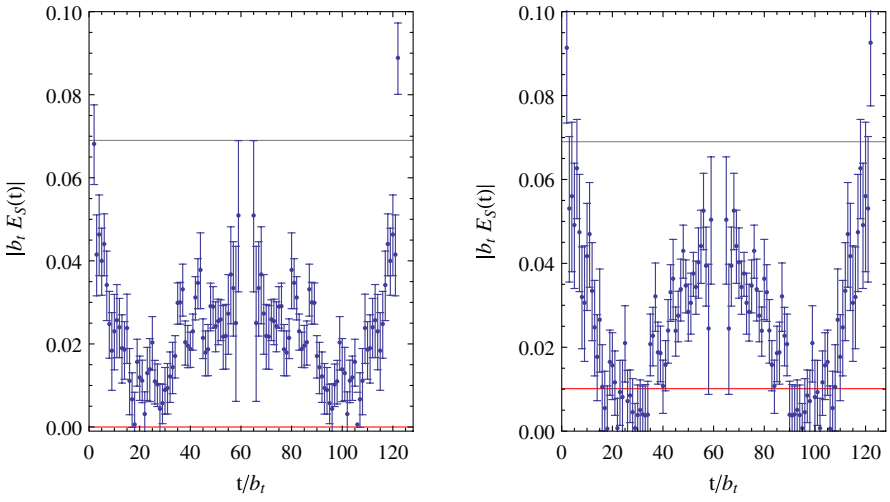

FIG. 29 (color online). The energy-scale, E_S, associated with the growth of the noise-to-signal ratio in the π^+ (left) and K^+ (right) smeared-smeared correlation functions using $t_J = 3$. The horizontal lines correspond (from lowest to highest) to 0, M_π for the pion and $M_K - \frac{1}{2}m_\eta - \frac{1}{2}m_K$ for the kaon.

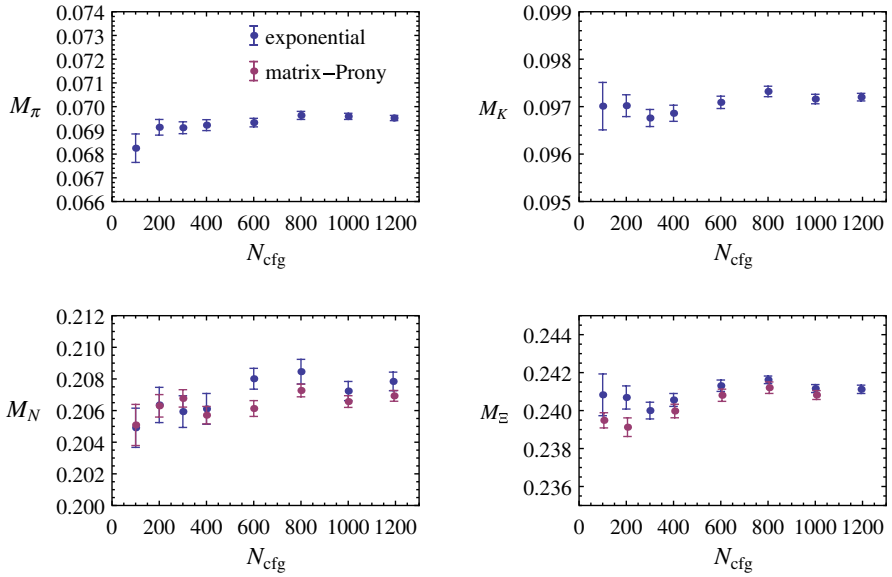

FIG. 30 (color online). The extracted masses of the π^+, K^+, N and Ξ as a function of the number of configurations (with the full set of measurements performed on it). Statistical and systematic uncertainties have been combined in quadrature. For the baryon states, both the matrix-Prony and exponential fits are shown.

worse scaling with the number of measurements per configuration in the case of the pion, consistent with the saturation seen in Fig. 3. This functional form enables us to quantify the relative benefit of increasing the number of sources per configuration compared to increasing the total number of configurations. The costs involved in this are as follows:

(i) *Gauge configuration generation*: The total cost of generating the ensemble of 1194 gauge configurations was 2 M JLab-6n cluster node-hours and the production took a significant amount of wall-clock time. Configuration generation costs scale linearly with the number of configurations once a Monte Carlo trajectory has thermalized (in this case the overhead of thermalization was approximately 10%). In order to generate significantly larger ensembles (containing 10^4 or 10^5 gauge fields) in a reasonable wall-clock time, it will be necessary to

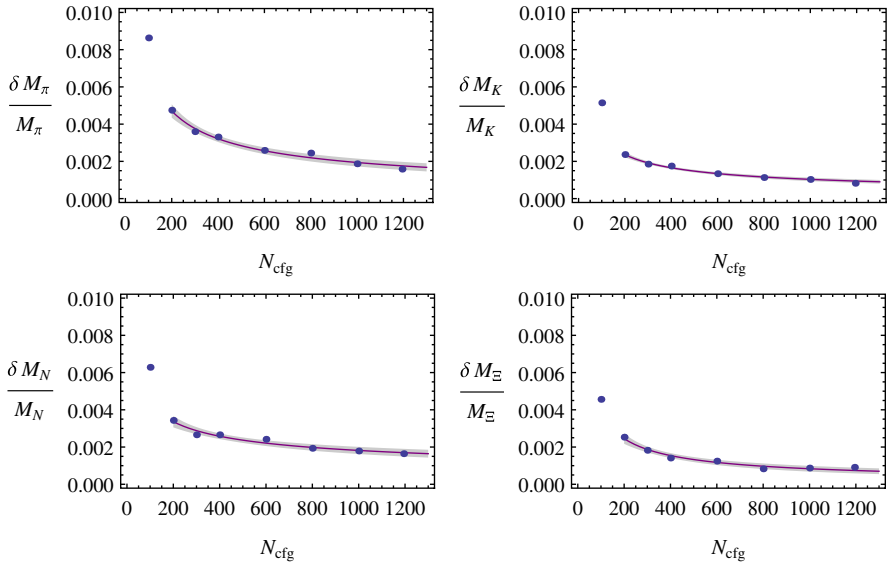

FIG. 31 (color online). The fractional uncertainty in the extracted masses of the π^+, K^+, N and Ξ as a function of the number of configurations (with the full set of measurements performed on it) for the exponential analysis. Statistical and systematic uncertainties have been combined in quadrature. The curves correspond to fits of the form $\delta M/M = AN_{\rm cfg}^b$. The exponents extract in these fits are $-0.55(4)$, $-0.51(3)$, $-0.38(4)$, $-0.67(6)$ for the π^+, K^+, N and Ξ, respectively.

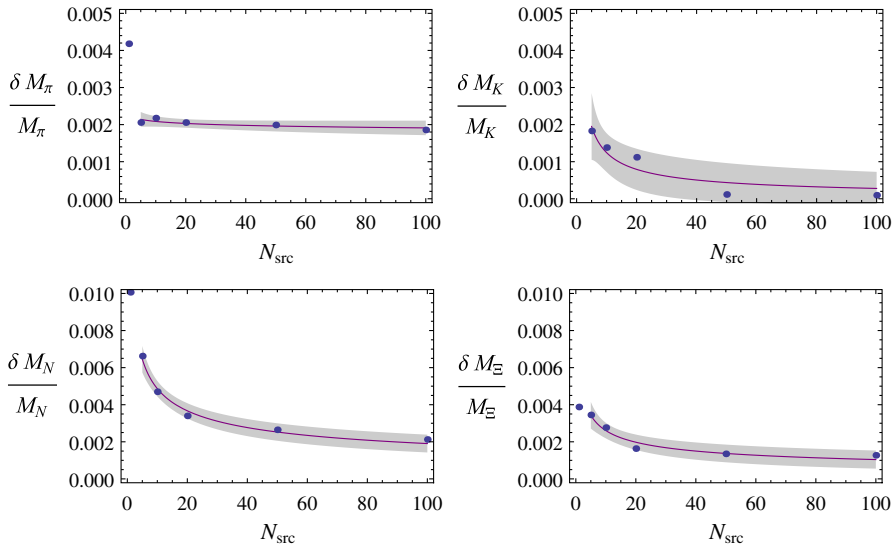

FIG. 32 (color online). The fractional uncertainty in the extracted masses of the π^+, K^+, N and Ξ as a function of the number of sources used on each configuration (1012 configurations were used in this study) for the exponential analysis. Statistical and systematic uncertainties have been combined in quadrature. The curves correspond to fits of the form $\delta M/M = AN_{\rm src}^b$. The exponents extract in these fits are $-0.03(2)$, $-0.65(19)$, $-0.41(3)$, and $-0.40(6)$ for the π^+, K^+, N and Ξ, respectively.

run multiple trajectories in parallel. Given wall-clock time and memory constraints, an individual trajectory will produce $\mathcal{O}(1000)$ gauge-field configurations that are useful for measurements. Consequently the thermalization overhead will conservatively remain at about 10%. Each configuration requires $\sim 2 \times 10^3$ JLab-6n node-hours to produce.

(ii) *Measurement calculations*: The total cost of computing all of the measurements performed in this work was 7×10^6 Jlab-6n node-hours. The cost to generate the 245 light-quark and strange-quark propagators per configuration on the 1194 configurations in this ensemble was ~3 M Jlab-6n node-hours, while the cost to generate the baryon and meson blocks (used at intermediate stages of the calculations) was ~3.5 M Jlab-6n node-hours. Contracting the blocks to accomplish the desired measurements (one, two, … baryons, one, two,… mesons and so forth) cost ~0.5 M Jlab-6n node-hours. If propagators on a given configuration are computed in sets of 100, the initial overhead of constructing deflation vectors in the EigCG algorithm becomes negligible (at the 1% level) and can be eliminated for further sets of calculations by storing the eigenvector information. On typical machines, each set of propagators and associated hadron blocks (technically, not an efficient way to calculated the single hadron spectrum, but critical for two and more hadron calculations) requires 22 JLab-6n node-hours to produce.

(iii) *Anisotropy:* The anisotropy of the lattices used in our calculations proved useful in reducing systematic errors in our fits (see Table III), providing approximately a $1/\sqrt{\xi_{\rm eff}}$ reduction. However, the cost of producing gauge-field configurations and propagators scales as approximately ξ^2 for the same physical extent (one power arises from the additional time slices and one power arises from the worsening condition number of the Dirac operator). Comparing these exponents, we would conclude that using anisotropic configurations is not ideal. However for more complicated multihadron systems where useful fit ranges are much reduced in physical units, the anisotropy will likely prove to be very useful. This remains to be investigated further in subsequent studies.

Using this information and the scalings in Eq. (47), we can address the question of how much computation is required to achieve a particular level of statistical precision. With the current data this is only possible in the single hadron sector; ongoing analyses will address the $B > 1$ in the near future. To halve the uncertainty in the determinations of the ground-state baryon masses (calculating the nucleon mass at the ~1 MeV-level), an increase in the number of configurations by a factor of four, or of the number of measurements per configuration by a factor of 5.6 is required. Achieving this precision by performing more measurements on the existing set of configurations (~ 1100 additional measurements on 1200 configurations) would cost 30 M JLab-6n node-hours. Achieving the same precision by generating an additional configurations and performing the same number of measurements on them (3600 configurations with 245 measurements) would require 27 M JLab-6n node-hours. Both approaches have similar cost at this level of precision, but for further improvements, the generation of additional configurations will be more efficient. Additionally, the second approach will further im-

prove the uncertainty for observables such as the pion mass that have saturated in terms of the number of sources per configuration. This approach would clearly be of more benefit to the broader community.

X. CONCLUSIONS

The energy-scales that arise in nuclear physics are typically in the MeV range, and in order for LQCD to have significant impact in this field, baryon masses (and energy-eigenstates in the volumes relevant to scattering processes) must be calculable with uncertainties that are a fraction of an MeV (including isospin-breaking and electromagnetic interactions, quark mass, lattice volume and lattice spacing extrapolations). Current computational resources do not permit such calculations. In this work we have performed the first high-statistics study of baryon correlation functions to better understand a number of issues that will impact the precision with which quantities of importance to nuclear physics can be determined with LQCD. In the future, we will extend our analysis to look at observables in the $B > 1$ baryon sector.

At the single lattice spacing, lattice volume and unphysical light-quark mass used in this work, we find the following set of ground-state masses

$$M_\pi = 390.3(0.7)(0.3)(2.5)\ \text{MeV},$$
$$M_K = 546.0(0.6)(0.2)(3.6)\ \text{MeV},$$
$$M_N = 1163.9(1.8)(0.6)(7.6)\ \text{MeV},$$
$$M_\Lambda = 1252.4(1.6)(0.3)(8.2)\ \text{MeV},$$
$$M_\Sigma = 1283.7(1.6)(1.0)(8.4)\ \text{MeV},$$
$$M_\Xi = 1356.1(1.4)(0.2)(8.8)\ \text{MeV},$$
$$E_{N(1/2^-)} = 1610(06)(11)(11)\ \text{MeV},$$
$$E_{\Lambda(1/2^-)} = 1679(05)(02)(11)\ \text{MeV},$$
$$E_{\Sigma(1/2^-)} = 1727(06)(06)(11)\ \text{MeV},$$
$$E_{\Xi(1/2^-)} = 1825(6)(5)(12)\ \text{MeV},$$

which we present in physical units. Since the lattice spacing is known with less precision than the lattice masses presented here, we make the systematic uncertainty arising from the lattice spacing explicit (third uncertainty). Given that there are significant ambiguities in scale setting, the most precise result will be for dimensionless quantities.

With high precision measurements of baryon correlation functions obtained from a single type of source for the light-quark and strange-quarks propagators, we have shown that the number of methods that can be used to extract the arguments of the contributing exponentials increases. This is due to the fact that some methods become stable when the uncertainties become small, such as the method of Prony and also the direct fitting of multiple exponentials. Histograms constructed from the roots found in the Prony method are found to be useful in identifying mass regions where states may exist, but we have not yet arrived at a well-defined (rigorous) method with which to use these histograms directly. It is likely that a more refined statistical analysis of these correlation functions using the most modern statistical tools will further increase the physics that can be extracted.

The exponential signal-to-noise degradation that plagues baryon correlation functions is currently a serious limitation for the calculation of nuclear physics observables, and is one significant difference between particle and nuclear physics LQCD calculations. The high-statistics calculations we have performed have allowed us to systematically explore this issue. We find that the issue is more serious than one would naively expect, due to (what in hindsight is now obvious) the use of antiperiodic BC's in the time direction on the quark-propagators. The variance of the correlation function is symmetric about the midpoint of the time direction of the configuration. Therefore, the optimal region in which to determine the baryon masses (and also their interactions) is in the first half of the configuration, far from the midpoint. This significantly reduces the number of useful time slices. Given that most the time required for these calculations is in the measurements, and not in the configuration generation, a cure for this problem is to generate ensembles of configurations that are longer in the time direction than those currently being used (as opposed to working with different BC's on the quark propagators that are less theoretically "clean").[9] The multiexponential fitting and Prony methods enable the ground-state to be probed closer to the source where the statistical uncertainties are exponentially smaller (also one of the important aspects of the variational method), somewhat reducing the impact of the exponentially degrading signal-to-noise near the midpoint of the configuration. Given that the signal-to-noise degradation is exponentially more severe in systems containing two or more baryons, all currently available tools will be required to make optimal use of the computational resources. For excited states in a given channel, variational methods seem to be superior to the standard approach used here.

An important result of this work has been to quantify the statistical scaling of simple observables in the subpercent regime of uncertainty. Scaling with the number of configurations was found to adhere to the expected $1/\sqrt{N_{\text{cfg}}}$ behavior. We have also investigated the issue of saturation, asking many measurements can be performed on a single gauge-field configuration before it becomes more cost effective to generate another statistically independent gauge-field configuration? To address this we have looked

[9]We note that combining quark propagators with both periodic and antiperiodic temporal BCs, to effectively double the length of the configurations as seen by the valence quarks, will not resolve all the noise issues as much of the problem is produced by states involving sea quarks which are encoded in the gauge configurations.

for deviations from $1/\sqrt{N_{\mathrm{src}}}$ behavior in the uncertainties in the correlation functions and extracted masses as a function of the number of measurements performed on each configuration in the ensemble. The measurements of the mesons start to saturate after a relatively small number of measurements, in this case of order ~ 10, while the baryon correlation functions show no signs of saturation up to ~ 200.

A natural question to ask is if the same extractions could have been performed with fewer computational resources by using the variational method with a number of different sources for the baryons. We estimate that comparable resources would have been required to achieve comparable uncertainties in the states we have examined. However, we have not been able to extract excited states of the nucleon with much precision because of closely-spaced states with the same quantum numbers. This is likely to be something that the variational method would better control. Given that the present work was exploratory in nature, this is not a concern at present, but it is clear that high-statistics calculations of correlation functions arising from multiple interpolating operators will be required in order to explore the structure and interactions of nuclei. We are working on implementing this, but it will require significant computational resources to perform, even at pion mass ~ 390 MeV and for a relatively small lattice volume and relatively coarse lattice spacing.

It is clear that sub-MeV uncertainties an hadron energies will become routine with the anticipated increase in computational resources available to lattice QCD, and that the small energy scales that characterize nuclear physics are within reach. However, this program will require large ensembles of gauge-field configurations that have large extent in the time direction, and will require a large fraction of the computational resources devoted to measurements.

ACKNOWLEDGMENTS

We thank R. Edwards and B. Joo for help with the QDP++/Chroma programming environment [14] with which the calculations discussed here were performed. K. O. would like to thank A. Stathopoulos useful discussion on numerical linear algebra issues and for his contribution in the development of the EigCG algorithm. EigCG development was supported in part by NSF grant CCF-0728915. We also thank the Hadron Spectrum Collaboration for permitting us to use the anisotropic gauge-field configurations, and extending the particular ensemble used herein. We gratefully acknowledge the computational time provided by NERSC (Office of Science of the U.S. Department of Energy, No. DE-AC02-05CH11231), the Institute for Nuclear Theory, Centro Nacional de Supercomputación (Barcelona, Spain), Lawrence Livermore National Laboratory, and the National Science Foundation through Teragrid resources provided by the National Center for Supercomputing Applications, and the Texas Advanced Computing Center. Computational support at Thomas Jefferson National Accelerator Facility and Fermi National Accelerator Laboratory was provided by the USQCD collaboration under *The Secret Life of a Quark*, a U.S. Department of Energy SciDAC project (http://www.scidac.gov/physics/quarks.html). The work of M. J. S. and W. D. was supported in part by the U.S. Department of Energy under Grant No. DE-FG03-97ER4014. The work of K. O. and W. D. was supported in part by the U.S. Department of Energy contract No. DE-AC05-06OR23177 (J. S. A.) and DOE grant DE-FG02-04ER41302. K. O. and A. W. L. were supported in part by the Jeffress Memorial Trust, grant J-813, DOE OJI grant DE-FG02-07ER41527. The work of S. R. B. and A. T. was supported in part by the National Science Foundation CAREER grant No. PHY-0645570. Part of this work was performed under the auspices of the US DOE by the University of California, Lawrence Livermore National Laboratory under Contract No. W-7405-Eng-48. The work of A. P. is partly supported by the Spanish Consolider-Ingenio 2010 Programme CPAN CSD2007-00042, by grants Nos. FIS2008-01661 from MEC (Spain) and FEDER and 2005SGR-00343 from Generalitat de Catalunya, and by the EU contract FLAVIAnet MRTN-CT-2006-035482.

[1] S. R. Beane, P. F. Bedaque, K. Orginos, and M. J. Savage (NPLQCD Collaboration), Phys. Rev. D **73**, 054503 (2006).
[2] S. R. Beane, T. C. Luu, K. Orginos, A. Parreno, M. J. Savage, A. Torok, and A. Walker-Loud, Phys. Rev. D **77**, 014505 (2008).
[3] S. R. Beane, W. Detmold, T. C. Luu, K. Orginos, M. J. Savage, and A. Torok, Phys. Rev. Lett. **100**, 082004 (2008).
[4] W. Detmold, M. J. Savage, A. Torok, S. R. Beane, T. C. Luu, K. Orginos, and A. Parreno, Phys. Rev. D **78**, 014507 (2008).
[5] W. Detmold, K. Orginos, M. J. Savage, and A. Walker-Loud, Phys. Rev. D **78**, 054514 (2008).
[6] L. Maiani and M. Testa, Phys. Lett. B **245**, 585 (1990).
[7] H. W. Hamber, E. Marinari, G. Parisi, and C. Rebbi, Nucl. Phys. **B225**, 475 (1983).
[8] M. Lüscher, Commun. Math. Phys. **105**, 153 (1986).
[9] M. Lüscher, Nucl. Phys. **B354**, 531 (1991).
[10] G. P. Lepage, in From Actions to Answers: Proceedings of

the TASI 1989, edited by T. Degrand and D. Toussaint (World Scientific, Singapore, 1990); QCD **161**, T45 (1989).
[11] H. W. Lin *et al.* (Hadron Spectrum Collaboration), Phys. Rev. D **79**, 034502 (2009).
[12] R. G. Edwards, B. Joo, and H. W. Lin, Phys. Rev. D **78**, 054501 (2008).
[13] A. Stathopoulos and K. Orginos, arXiv:0707.0131.
[14] R. G. Edwards and B. Joo (SciDAC Collaboration), Nucl. Phys. B, Proc. Suppl. **140**, 832 (2005).
[15] M. Teper, Phys. Lett. B **183**, 345 (1987).
[16] M. Albanese *et al.*, Phys. Lett. B **192**, 163 (1987).
[17] C. Morningstar and M. J. Peardon, Phys. Rev. D **69**, 054501 (2004).
[18] R. G. Edwards and B. Joo, (private communication).
[19] S. Prelovsek and D. Mohler, Phys. Rev. D **79**, 014503 (2009).
[20] W. Detmold, C. J. Lin, and M. Wingate, arXiv:0812.2583.
[21] J. Juge, private communication.
[22] C. Michael, Nucl. Phys. **B259**, 58 (1985).
[23] M. Lüscher and U. Wolff, Nucl. Phys. **B339**, 222 (1990).
[24] G. T. Fleming, arXiv:hep-lat/0403023.
[25] F. B. Hildebrand, *Introduction to Numerical Analysis* (Dover, New York, 1987), 2nd ed..
[26] G. R. de Prony, Journal de l'École Polytechnique **1**, cahier 22, 24 (1795).
[27] H. W. Lin and S. D. Cohen, arXiv:0709.1902.
[28] G. T. Fleming, S. D. Cohen, H. W. Lin, and V. Pereyra, arXiv:0903.2314.
[29] M. R. Osborne and G. K. Smyth, SIAM J. Sci. Statist. Comput. **16**, 119 (1995).
[30] G. T. Fleming, S. D. Cohen, H. W. Lin, and V. Pereyra, Proc. Sci., LAT2007 (2007) 096.
[31] B. Smigielski and J. Wasem, Phys. Rev. D **79**, 054506 (2009).